Journal of Physics: Condensed Matter

TOPICAL REVIEW

In situ and *ex situ* NMR for battery research

IOP Publishing Journal of Physics: Condensed Matter
J. Phys.: Condens. Matter **30** (2018) 463001 (25pp) https://doi.org/10.1088/1361-648X/aae5b8

Topical Review

In situ and *ex situ* NMR for battery research

Jian Zhi Hu[1,2], Nicholas R Jaegers[1], Mary Y Hu and Karl Todd Mueller[2]

Pacific Northwest National Laboratory, The Joint Center for Energy Storage Research (JCESR), Richland, WA 99352, United States of America

E-mail: Jianzhi.Hu@pnnl.gov and Karl.Mueller@pnnl.gov

Received 10 November 2017, revised 20 September 2018
Accepted for publication 2 October 2018
Published 30 October 2018

Abstract

A rechargeable battery stores readily convertible chemical energy to operate a variety of devices such as mobile phones, laptop computers, electric automobiles, etc. A battery generally consists of four components: a cathode, an anode, a separator and electrolytes. The properties of these components jointly determine the safety, the lifetime, and the electrochemical performance. They also include, but are not limited to, the power density and the charge as well as the recharge time/rate associated with a battery system. An extensive amount of research is dedicated to understanding the physical and chemical properties associated with each of the four components aimed at developing new generations of battery systems with greatly enhanced safety and electrochemical performance at a significantly reduced cost for large scale applications. Advanced characterization tools are a prerequisite to fundamentally understanding battery materials. Considering that some of the key electrochemical processes can only exist under *in situ* conditions, which can only be captured under working battery conditions when electric wires are attached and current and voltage are applied, make *in situ* detection critical. Nuclear magnetic resonance (NMR), a non-invasive and atomic specific tool, is capable of detecting all phases, including crystalline, amorphous, liquid and gaseous phases simultaneously and is ideal for *in situ* detection on a working battery system. *Ex situ* NMR on the other hand can provide more detailed molecular or structural information on stable species with better spectral resolution and sensitivity. The combination of *in situ* and *ex situ* NMR, thus, offers a powerful tool for investigating the detailed electrochemistry in batteries.

Keywords: energy storage, batteries, multi-nuclear NMR, ^{7}Li, ^{133}Cs, ^{17}O, ^{25}Mg, Magic angle spinning NMR, solvation structures, computational modeling

(Some figures may appear in colour only in the online journal)

1. Introduction

The efficient storage of energy has seen a remarkable escalation in importance as an increasingly mobile and energy-demanding global population arises. Since the first voltaic piles were produced over 200 years ago, progressive improvements to this technology have been made to decrease the size, increase the capacity, lengthen the service life, and even allow for the reuse of the cell. Due to the convenience of recharging, batteries, in particular Li–ion batteries, have become the dominant power source for portable electronic devices and mobile electrically-powered vehicles [1, 2]. Consumer demand for devices with enhanced power cycle lifetimes has driven the development of rechargeable batteries with continually increasing energy density. As these improvements are realized, a given battery class may reach the theoretical maximum energy density limit, requiring the use of different

[1] Authors contributed equally.
[2] To whom correspondence should be made.

internal materials for continued progress. As such, extensive research efforts have focused on improving the performance of these energy storage devices by utilizing alternative materials within the battery. Judicious electrochemical improvements require a thorough understanding of the chemical interactions taking place within the battery, prompting a need for thorough scientific research into these technologies.

The chemistry of batteries occurs with four basic components: two electrodes (cathode and anode), a separator, and an electrolyte. The anode (negative terminal) serves as the source of electrons in the electric circuit. The cathode (positive terminal) accepts these electrons. The electrons are transferred through the electrolyte as ions, allowing for the flow of current. Each of the electrolyte constituents (i.e. solvent, salts and other additives) has a dramatic impact on the performance of the battery and can impact the chemistry of the other materials. The operation of a battery is reliant upon electron and ion transfer across solid–solid and solid–liquid interfaces. Within a given phase, changes in one component can impact the response of electron and ion transfer as well as the reversibility. For rechargeable battery systems, the repeated cycling induces the formation of microstructures at the solid-electrolyte interface (SEI) as well as in the electrode itself due to the migration of ionic species, which is often responsible for battery failure. Thus, it is necessary to have a deep understanding of each component and how they will impact the battery's performance.

The physical and chemical properties of electrolytes are directly derived from the composition of the electrolyte. Maximizing the conductivity, ionic fluidity, non-reactivity with electrodes, and stable operating temperature range are important attributes of an electrolyte. Anodes should be efficient reducing agents that exhibit good conductivity, high coulombic output, and stability. Cathodes, on the other hand, should be efficient oxidizing agents over the desired voltage and stable when in contact with the electrolyte. The separator is a porous membrane that prevents the direct contact of the two electrodes. It must be stable under the reactive conditions and uniformly permeable to the ions or electrolytes carrying the ions.

There exist a number of important considerations regarding the electrode design beyond electrochemical potential. On one hand, the formation of soluble intermediate species is critical to harnessing the power of the cell, but dissolved species can also be an indicator of failure, requiring the use of carefully designed materials to limit the diffusion of soluble species, as in the case of utilizing sulfur-impregnated carbon nanotubes as a cathode to mitigate diffusion and improve cycle stability [3]. Refinements to the design of electrodes can also be made to prevent significant volumetric expansion of the cell, which is highly undesirable in commercial applications. In one such example, a sulfur-titania yolk-shell architecture was used to preemptively provide void space for volumetric expansion [4]. Other architectures can be envisioned to improve the conductivity of the electrodes [5].

Despite these efforts, there is still much to learn about the species generated on electrodes and in the SEI during operation. Their nature and the mechanisms by which these microstructures arise are difficult to ascertain. Further, the specific reasons for a given electrolyte showing promising performance over another are not always intuitive, requiring careful molecular level experimental observations to understand the fundamental principles at work. The SEI is often poorly understood as well, despite being a key component in advanced electrochemical devices. This interface forms as solvent and electrolyte salts are reduced to oligomers and crystals on the electrode surface. These electrolytes are stabilized at potentials beyond their thermodynamic limits, enabling the reversibility of the reaction. However, the chemistry, formation mechanism, and cycle-induced evolution of these are largely unknown, promoting a strong desire for detailed investigations [6].

A variety of techniques have been employed to evaluate the performance and chemistry of batteries to better understand their operation and failure mechanisms for continued enhancements to performance. Techniques unrelated to nuclear magnetic resonance (NMR) have provided excellent insight for battery technology. Many of these methods will be briefly discussed to provide an overview of the insight they provide. Cyclic voltammetry, for instance, is extensively used to characterize the general electrochemical performance of a battery, such as the stability and reversibility of the reaction at a given potential [7]. More detailed analysis allows for a measurement of the electrode reaction kinetics [8]. This technique, however, fails to provide a clear and detailed picture of the molecular changes that occur throughout the repetitive cycling process. In particular, this technique lacks a decisive description of the chemical evolution of the various battery components and how this dynamic process impacts the properties of the cell.

Beyond the standard electrochemical performance evaluations, characterization of the materials encourages a deeper understanding of system limitations and potential enhancement routes. One such avenue for characterization is the direct imaging of the battery with microscopy techniques [9, 10]. The advent of highly-developed aberration-corrected scanning and transmission electron microscopy (TEM) has propelled the capability to atomic-scale imaging [11–16]. *Ex situ* beam imaging has been widely applied to analyze the structural features of battery constituents, but failed to capture information related to the dynamics of the charge/discharge cycles [17–19]. *In situ* investigation of batteries with TEM is challenging owning to the high-vacuum operation of the equipment and subsequent incompatibility with liquid electrolytes. To mitigate this, three strategies have been explored to provide an *in situ* analysis of these materials. The first, an open-cell configuration utilizing ionic liquid-based electrolytes, takes advantage of nanowire anodes that are wetted by the ionic liquid to mimic an electrolyte system [20, 21]. It has been used to study a number of anode materials, including Si, Ge, Al_2O_3, SnO_2, ZnO, graphene, Sn, and carbon nanotubes [22–28]. This concept, however, suffers from ionic liquid polymerization in the presence of the electron beam, significantly shortening the number of charge/discharge cycles allowable by the system. The next, another open-cell configuration but using metal and metal oxide electrolytes, has been used for Li metal and silicon electrodes with a lithium oxide electrolyte [29]. Variations

exist, but this design can be used with Na-, Mg-, and Ca–ion battery systems as well [30, 31]. Again, this configuration is not representative of a truly rechargeable battery due to limitations on the charging cycles and beam-induced effects, but these open cell configurations offer significant advantages in spatial resolution imaging and chemical analysis by electron energy loss spectroscopy [31]. Finally, a closed liquid cell battery design has been employed to better mimic the electrolyte diffusion and electrode interaction characteristics exhibited in a typical cell. Initiated by studies on copper nanoparticle growth from an electrolyte solution, electrochemical cells for *in situ* TEM were developed to push the technology forward [32, 33]. Working battery cells soon followed that allowed for the direct observation of the lithiation, ion transport, and SEI layer formation [34–37]. However, replicating a realistic number of charge/discharge cycles is still a concern with this technology. In addition to these, liquid observation is also possible to monitor changes in electrolytes, but further development in the field is required to match the performance of analyzing the solid components [10].

Raman spectroscopy can also be used to characterize changes in battery components. *Ex situ* Raman spectroscopy and ellipsometry have been employed to characterize the carbon films used as electrodes in Li–ion cells [38]. For example, they have shown that the structure of different carbon samples is degraded slightly through progressive discharge cycles. In addition to observing changes to the carbon anodes, cathodic $LiCoO_2$ rock-salts have been shown to deintercalate lithium species and result in seemingly random Li^+ occupations of the available sites on the lattice [39]. In addition to the information *ex situ* Raman can offer, *in situ* Raman sampling cells have also been employed to observe the specific cycling stages in which intercalation of electrolyte ions into graphitic electrodes occurs [40, 41]. For instance, similar technologies have been used to show the specific redox steps proceeding at given voltage transitions for Li–ion and Li–S batteries, for example [42, 43]. Surface reaction mechanisms at the electrolyte-electrode interface can be probed as well, as was performed for Li–ion and Li–V_2O_5 systems [44–46]. It has even been used to show the complex and oscillatory distribution of ions in various regions of the separator and other fragments of the battery [47, 48]. UV–vis spectroscopy has also been shown to provide quantitative evidence on the polysulfide chain growth during Li–S battery operation [49]. Similarly, infrared methods have played a role in better understanding the nature of the SEI [50, 51]. These real-time capabilities have notably contributed to a deeper understanding of the changes that occur within the battery.

A number of x-ray methods have contributed to the scientific understanding of battery systems by analyzing samples both *in situ* and *ex situ* [52]. X-ray diffraction (XRD), for instance, can be used to understand the phase and layer spacing of electrodes [53]. An early demonstration of *in situ* XRD measurements for electrochemical applications focused on understanding the phases generated during the intercalation of lithium into graphite during electrochemical cycling [54]. This work studied various $Li:C_6$ ratios and found a random distribution of Li at low Li content with more distinct phases arising with the intensification of metal content, accompanied by an increasing carbon layer spacing as the lithium content increased. Utilizing synchrotron radiation and a specially designed cell, Walus *et al* were able to separate the diffraction pattern contributions from individual electrodes in a Li–S battery from the signal of the entire cell [55]. This demonstrated the formation of Li_2S on the anode at the early stages of the discharge cycle and complete consumption during the subsequent charge. Additionally, XRD was used to demonstrate the formation of a different sulphur allotrope after recrystallization. Numerous additional *in situ* XRD studies have focused on the crystalline phases present for a variety of battery systems; Li–Si, Li–MO_x, Li–air, Li–ion, Na–ion, etc [56–63]. An *in situ* XANES cell has also been used, though less commonly due to the necessity of a synchrotron, to investigate electrodes and electrolytes for sulfur speciation on the sulfur K-edge, showing the impact of sulfur species on capacity [64, 65].

X-ray photoelectron spectroscopy (XPS) and Auger electron spectroscopy (AES) have been used both *in situ* and *ex situ* to understand the bonding and oxidation state of the electrodes throughout the cycling process, but these techniques suffer from drawbacks related to the need to operate under ultra-high vacuum (UHV) conditions and difficulties with mitigating the relevance of closed cell designs with open cell detection sensibility [66, 67]. To address the concern about operating under UHV conditions, recent XPS efforts on Li–air battery research take advantage of a special *in situ* 'ambient pressure' cell that allows for reaction monitoring up to 500 mtorr (0.0007 bar), which demonstrated notable differences in the Li species present upon discharge as compared to UHV studies [68]. Though an impressive improvement, this pressure falls significantly short of ambient (1 bar). Despite these shortfalls in realistic condition representation, key insights have been gained from employing the technique with complementary experiments [69–71]. Additionally, XPS benefits from the ability to detect the presence of organic impurities on the electrode surface that arise from power cycling [72].

In situ and *ex situ* NMR spectroscopies have contributed significantly to the field. NMR allows detailed molecular level information related to electrolyte, separator, and electrodes all to be observed if contained within the detection RF (radio frequency) coil. Although not without its own limitations in sensitivity, it holds many unique advantages and has been thoughtfully developed over the last two decades. For one, NMR is (generally) a quantitative technique that allows for tracking the concentration of species regardless if they are liquid, solid, gaseous phases or a mixture of these phases from sample to sample or over time as the electrochemical reaction proceeds. For solid phases, both the amorphous and the crystalline phase can be captured at the same time. It should be noted that quantitative measurements are limited to skin depth when applied to metals and thus the thickness of the microstructure and bulk surface area must be considered [73]. Another significant advantage to NMR is that it is non-destructive, allowing non-invasive detection of the process under true *in situ* conditions where unique species may only exist. The true *in situ* conditions include, but are not limited to, operating at a wide temperature range, e.g. from well

below 0 °C to well over 100 °C, and operating at pressures ranging from well below ambient to 100 bars and above [74–77]. Furthermore, the layout of the battery components and the size of the battery can be made the same as commercially available mini-sized batteries. The only exception here is that the outmost stainless container is replaced by a plastic holder to allow the RF field to penetrate into the battery electrodes, separator and electrolytes. In combining the *in situ* NMR with the detailed molecular information of stable species obtained by *ex situ* methods, NMR can be an invaluable addition to the experimental arsenal of a battery investigation [78–80].

Two additional differences between characterization by NMR and other techniques are the intrinsic length and time scales of the measurements performed. Herein, we seek to provide an overview of these scales for NMR, but would refer the reader to other literature on the spatial and temporal limits of other methods [81]. The time scale associated with NMR is not a straight-forward, singular concept. In fact, it should be regarded as a collection of scales due to the abundance of phenomena that this spectroscopy technique may probe. While changes to specific chemical signals can be monitored during a process, the mobility of these species and their interactions with surrounding media reveal unique transient information. These phenomena will be discussed to give the reader a sense of the capabilities NMR processes that can be employed to better understand battery systems.

The local chemical environment of the nucleus being analyzed directly impacts observed chemical shifts. Such a measure for the local environment relinquishes insight on the bonding structure and lengths, torsion angles, hydrogen bonding networks, secondary structures, and electric charges [82]. Due to the multiple factors determining the observed frequency, theoretical calculations that simulate bonding structure and secondary structures are often necessary for a deeper interpretation of the observed signals. Such calculations have shown the important impact of a second solvation shell on the observed solute chemical shifts, suggesting a length scale on the order of nm [83]. Nucleus-electron coupling has also been shown to impact NMR signals, suggesting a range of a few angstroms [84]. Further lengths scales could arise from the molecular motion of the nucleus itself as it is exposed to different environments. Environment-specific information is commonly used to provide dynamic speciation of observed signals. Though it has relatively low temporal resolution, chemical species transformation during a time-lapsed *in situ* experiment is one direct measure of the time scale for NMR spectroscopy. This type of experiment monitors changes in the chemical structure over a period of time. For example, in section 5.3 (titled In situ NMR on Li–ion battery research) we recount the evolution of ^{7}Li species on the electrode during electrochemical cycling and highlight the changes in species identity over time. The time scale to analyze such transformations is heavily dependent upon the system. Factors such as the nucleus, relaxation environment, spin abundance, and experiment type all play an important role in determining the minimum time for analysis. This type of experiment can be conducted on a wide range of time scales, typically on the order of seconds (or fractions of a second) for an abundant ^{1}H system to hours or even days on a less favorable nucleus. Similar time resolutions (though often extended) can be applied to observe the change (or derivative) of other transient behaviors described, such as a change in the chemical exchange rate during a reaction.

In addition to the chemical shift value describing length-based information, the linewidth of a given signal provides the dynamic properties of a molecule, such as the rotational and translational behaviors. Though related to the relaxation mechanisms (see below), this motion is also related to the interchanging of species environment. This phenomenon is termed chemical exchange and is readily elucidated by NMR [85]. In this, a given nucleus may sample a range of magnetic environments, such as an interchanging ligand state, during the exchange process and the resulting NMR spectrum will provide kinetic data on the exchange rate. The concept is analogous to the uncertainty principle whereby the uncertainty in the resonance frequency is inversely proportional to the lifetime in a given state. For instance, when the exchange rate is relatively high, the lifetime in a given state is low and the resonant frequency is apparent. The temporal limitations of chemical exchange are determined by the frequency difference between two species, and thus the nucleus and magnetic field, according to equation (1).

$$\tau_{\text{coalescense}} = \left(\sqrt{2}\pi\Delta\nu\right)^{-1} = k^{-1}. \tag{1}$$

Here, $\Delta\nu$ represents the frequency difference between the magnetic environments. For a slowly exchanging process, each resonance is well-resolved. Exchange spectroscopy (EXSY) has been used in this regime to quantify dynamics on the ms time scale [86]. As the exchange rate increases, the lines broaden and migrate towards the weighted average signal location. When the exchange rate reaches about an order of magnitude higher than the frequency difference, the resonances are averaged to a single broad line. On this time scale, fractions of ms, the Carr–Purcell Meiboom–Gill relaxation dispersion (CPMG RD) approach can be applied to refocus the exchange broadening with the spin-echo pulse sequence to elucidate the relationship between this observed broadening and the exchange rate [87]. This single line narrows to reveal a sharper resonance up until about three orders of magnitude faster exchange than the frequency difference [88]. To visualize the range of time scales for the exchange process, the reader can imagine the case of two resonances at the extremes of a given nucleus' chemical shift range. The time scale involved in the averaging of these two species can be approximated by equation (1), bearing in mind the effect of magnetic field on the frequency difference. As shown in table 1, the NMR time scale for ^{1}H exchange at 7 T varies from 0.2 s (given 1 Hz resolution) down to 58 μs for the full range of 3.9 Hz. Since the frequency range (columns 3 and 5) vary based on the field strength, so too does the NMR time scale for exchange, where a proportional reduction is observed between columns 4 and 6.

Table 1. Representative chemical shift ranges and times scales for nuclei at two magnetic fields.

Nucleus	Approx. shift range, ppm	Shifts at 7 T, kHz	7 T time scale	Shifts at 19.9 T, kHz	19.9 T time scale
^{1}H	13	0–3.9	0.2 s–57.7 μs	0–11.1	0.2 s–20.4 μs
^{2}H	13	0–0.6	0.2 s–0.4 ms	0–1.7	0.2 s–0.1 ms
^{6}Li	28	0–1.2	0.2 s–0.2 ms	0–3.5	0.2 s–64.2 μs
^{7}Li	28	0–3.3	0.2 s–68.9 μs	0–9.3	0.2 s–24.3 μs
^{13}C	200	0–15.1	0.2 s–14.9 μs	0–42.8	0.2 s–5.3 μs
^{15}N	900	0–27.4	0.2 s–8.2 μs	0–77.6	0.2 s–2.9 μs
^{17}O	1160	0–47.2	0.2 s–4.8 μs	0–133.7	0.2 s–1.7 μs
^{19}F	300	0–84.7	0.2 s–2.7 μs	0–240	0.2 s–0.9 μs
^{25}Mg	70	0–5.6	0.2 s–40.5 μs	0–15.7	0.2 s–14.3 μs
^{29}Si	519	0–30.9	0.2 s–7.3 μs	0–87.7	0.2 s–2.6 μs
^{31}P	700	0–85	0.2 s–2.6 μs	0–241	0.2 s–0.9 μs
^{51}V	1900	0–150	0.2 s–1.5 μs	0–425	0.2 s–0.5 μs
^{133}Cs	160	0–6.3	0.2 s–35.7 μs	0–17.8	0.2 s–12.6 μs

The observation of dipole-dipole coupling by NMR can also indicate the time scale of molecular motion. The scalar coupling constant can be applied to equation (1) to provide the threshold for the exchange rate. If the lifetime of the species in a given environment is short compared to the inverse of the coupling constant, no coupling will be observed in favor of a single resonance. Typical coupling constants for ^{1}H–^{1}H, ^{13}C–^{1}H, and ^{15}N–^{1}H may be around 10, 150, and 50 Hz. These correspond to about 22, 1.5, and 4.5 ms, respectively, though this can be reduced to the ps time scale in specialized applications [89]. Since J-coupling is not impacted by field, these time scales are field independent and directly impacted by the chemical bonding.

In addition to gaining insight on the time scales involved with dynamic chemical environments, NMR is widely used to study the relaxation time scales of chemical species. T_1, for instance, is a measure of the longitudinal NMR relaxation that describes the rate in which excited nuclear states relax to equilibrium magnetization in the direction of the applied field. This relaxation is governed by modulation of the nuclear spin energy levels from fluctuations in magnetic interactions with components that match the Larmor frequency of the nucleus. This could arise from such physical processes as vibrations, torsion angle rotations, and looping motions [88]. The spin-lattice dipolar relaxation rate (reciprocal time) is described by equation (2) and shows a maximum rate at $\omega\tau_C = 0.6158$, where ω is the resonant frequency and τ_C is the correlation time [90]. Though an indirect measure of the time scale, it is important to note that it is dependent upon the Larmor frequency, and thus the magnetic field, where the time scale of molecular motion associated with this relaxation is on the order of $(2\pi\Upsilon)^{-1}$. Though spin-lattice relaxation times are typically on the order of seconds, the corresponding time scale for molecular motion (translation, rotation, or vibration) is on the order of 0.1–10 ns. In considering the relaxation initiated by paramagnetic centers, such as a rotating metal complex, the time scale for this motion can extend down to tens of picoseconds [91]. On a similar time order, but often smaller in magnitude to the spin-lattice relaxation time, transverse relaxation via spin-spin interactions can similarly be detected. The characteristic dipolar equation describing T_2 can be found in equation (3). Further system insight can be obtained through measurements of the two relaxation rates. Through this, time scale uncertainties can be drastically reduced to reveal the correlation time between species, $\tau_{C.}$

$$\frac{1}{T_1} = \frac{3}{160}\frac{\mu_0\gamma^4\hbar^2}{r^6}\left[\frac{\tau_C}{1+\omega^2\tau_C^2} + \frac{4\tau_C}{1+4\omega^2\tau_C^2}\right] \quad (2)$$

$$\frac{1}{T_2} = \frac{3}{320}\frac{\mu_0\gamma^4\hbar^2}{r^6}\left[3\tau_C + \frac{5\tau_C}{1+\omega^2\tau_C^2} + \frac{2\tau_C}{1+4\omega^2\tau_C^2}\right] \quad (3)$$

where γ is the gyromagnetic ratio (rad/s/T), $\hbar$ is the reduced Plank's constant ($1.054\,56 \times 10^{-34}$ m^2 kg s^{-1}), ω is the Larmor frequeny (s^{-1}), and μ_0 is the magnetic permeability of free space (1.2566×10^{-6} H m^{-1}). Transverse relaxation in the rotating frame can also be employed to elucidate the time scale for fast exchange rates that are challenging to determine by other methods (such as CPMG) due to the maximum pulsing rate [92]. For these high exchange rates, a technique exists that enables the determination of $T_{1\rho}$. This approach is further advantaged by the enhanced sensitivity of minor species in an exchange process and by the requirement of only one static field strength. This method provides the potential to identify exchange rates on the order of ms to μs [93]. The interested reader is directed to other sources for details on the pulsing schemes for $T_{1\rho}$ determination [94].

Given the variety of mechanisms by which NMR can provide insight into the time scales of the chemical interactions, it can certainly be considered an attractive option to probe chemical systems. Though this review and many published works primarily analyze the time scales associated with changes to the species identity (chemical shift), the framework for additional insight exists, demonstrating the power for NMR to supply a wealth of information about chemical systems *in situ*. Figure 1 provides a summary of the applicable time scales for NMR.

A recent review by the Grey group has described their own thorough endeavors related to NMR spectroscopy applied to batteries [95]. The article outlines the purpose for utilizing

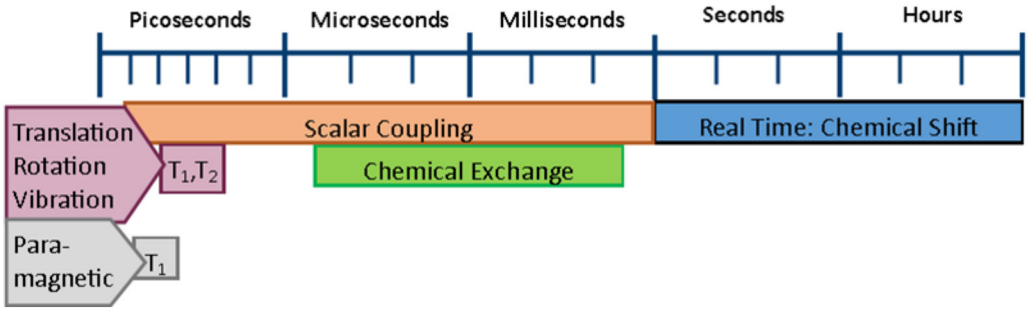

Figure 1. Sketch of time scale summary.

NMR spectroscopy to understand battery systems as well as specific instructions for sample and experimental preparation and design. Other battery-class specific reviews are described in the relevant sections. Herein, we describe the development of *in situ* and *ex situ* solid-state NMR for battery research and discuss key examples that highlight the power of NMR in battery research. The included examples are specifically centered on chemical shift-structure relationships to identify the types of species present in batteries and electrolytes. These methods are complimented with computational chemistry to make accurate assignments of the observed spectral featured. An understanding of the temporal resolution on the time scale of several seconds and higher is described to monitor the chemical transformations during cycling.

2. *In situ* NMR technologies

Distinct advantages present themselves in conducting *in situ* observation. Apart from the advantage of observing the state of the material during the entire process instead of only discrete stages of a transformation, *in situ* investigation does not require numerous samples to be prepared for a full understanding of an entire process, saving time and promoting sample consistency. Instead, one representative sample can be scanned throughout the entire process. Importantly, some transient species can only exist when the electric wires are attached to the battery systems with current constantly applied [96, 97]. There are, however, technical challenges in successfully devising an apparatus suitable for *in situ* investigation. A number of iterations have taken place to promote *in situ* capabilities that have better reliability, sensitivity, and longevity.

The first demonstration of *in situ* NMR for batteries came from technology developed by Rathke *et al* at Argonne National Laboratory [98]. Their design employed a toroid cavity in their custom built probe similar to that developed for magnetic resonance imaging [99, 100]. The first battery experiments used Li–ion coin and cylindrical cell containers that integrated operation with the RF coil [101, 102]. This was an exciting advancement that allowed for ^{7}Li NMR observations on a live battery system where charge-discharge cycling took place directly in the magnet. The drawback on employing the toroid coil was that the same copper disc (or central wire) was simultaneously used as both the current collector and radio frequency conductor for NMR signal excitation and detection. This means that for *in situ* measurement to begin, the battery operation had to stop periodically or non-periodically. Still, the battery was charged and discharged within the probe and magnet and measurements were taken shortly after the cycling was stopped, but this was a severe limitation in terms of truly *in situ* measurement.

Though the toroid design for *in situ* experiments provided a new frontier for the investigation of a functioning battery, it suffered from challenges in conformity with standard (lithium ion) battery designs in addition to severely limited signal-to-noise ratios. In the mid-nineties, small, flexible, plastic Li–ion batteries with the capability of being recharged were demonstrated by Bellcore, offering improved application flexibility [103]. To address the aforementioned disadvantages of the toroid design, this plastic cell design was sized for utilization as an *in situ* NMR cell by Chevallier *et al* in Orléans, France in 2003 [104]. This allowed for direct use inside an NMR probe for truly *in situ* electrochemical cycling since recording in open-circuit mode was no longer a limitation [105]. A schematic of the plastic bag cell and the accompanying detection and cycling system is shown in figure 2. In this design, each electrode was supported on a copper current collector before being treated in a 1% solution of polyvinylidene fluoride-hexaflouropropylene (PVDF-HFP) in acetone and laminated (130 °C, 20 psi) to opposite sides of a separator membrane composite composed of PVDF-HFP and dibutyl phthalate. With the stack activated with electrolyte prior to the second electrode being laminated to the separator, the two electrodes, separated by a membrane and resting between current collectors, were then packaged into an ultra-thin aluminum blue bag measuring 4 cm by 8 mm. These plastic bag cells provided a low cost and flexible option for *in situ* measurement, but experienced relatively short lifetimes (five days has been reported) due to cell breakage and permeability. The cells can also experience large electrical resistance [106]. Al-coated bags have been used to extend the cell lifetime, but these decrease the sensitivity of the experiment [105]. Early demonstrations of ^{7}Li *in situ* NMR for battery technology with these plastic cells allowed for up to 2 mg of Li and 16.7 mg of graphite to be involved in the intercalation process [107]. This design allowed for the successful observation of reversible lithium intercalation into the carbon layer, where a direct charge transfer from lithium is realized. After the formation of these intercalated species, lithium is capable of penetrating the graphitic nanopores to form quasi-metallic species that registered downfield [104]. It has also allowed for

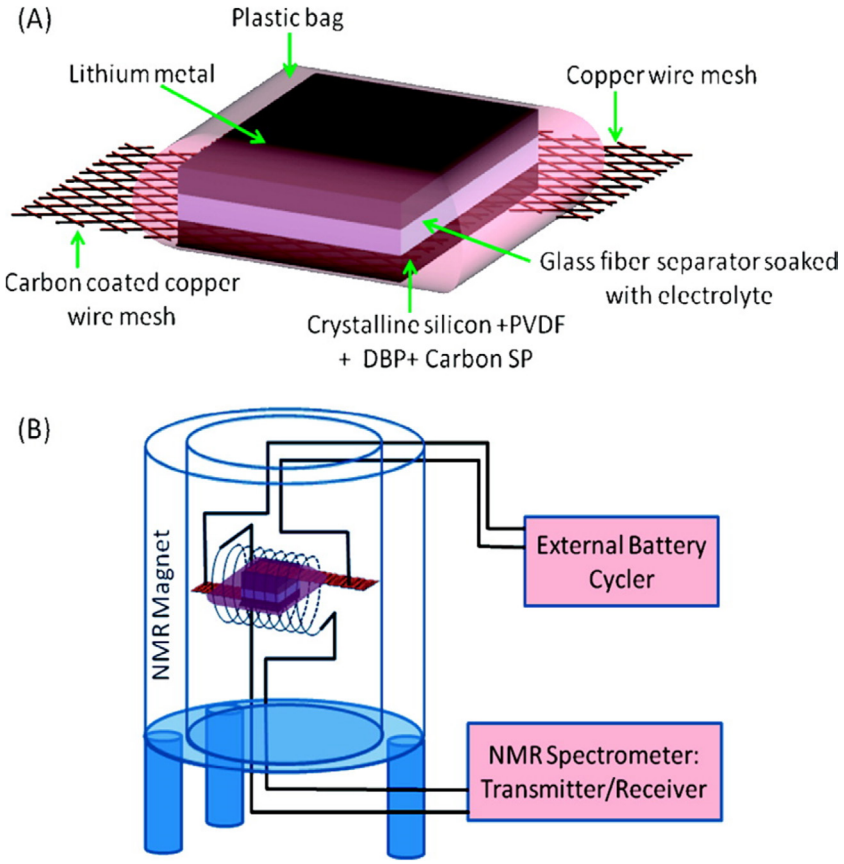

Figure 2. (A) Schematics of the flexible plastic battery used for the *in situ* static NMR experiment and (B) the *in situ* static NMR setup. A similar, but more detailed schematic with photographs has been published by Pecher *et al* [106]. Reprinted from [106], Copyright 2016, with permission from Elsevier. Reprinted with permission from [115]. Copyright 2009 American Chemical Society.

the firm identification of the dense interstitial LiC_6 and LiC_{12} as well as clarified the true identity of the dilute LiC_9 stage, demonstrating the importance of careful sample preparation (washing stage) for the *ex situ* NMR data collected in the decades prior [108–110].

While the flat plastic cell propelled *in situ* NMR for battery applications and reduced the metallic components contained within, it suffered from key drawbacks such as the restriction to plastic electrodes and fragility that leads to solvent leakage and a loss of electrical contact. To address this, an improved design made especially for Li–ion batteries was constructed from a cylindrical plastic housing with a threaded seal, reducing the sealing area and metallic components while providing good cycling characteristics, as demonstrated with ^{31}P NMR for on Cu_3P electrode in the Li–ion battery [111]. Another design is based on a cylindrical micro-battery developed for a telemetry system for salmon tracking [112]. This jelly roll structure was subsequently used to study Li–S batteries where the Kel-F holder containing the battery cell sat directly inside the RF coil and a charge cycler could be connected to the apparatus outside of the magnet [96]. Similar versions of the cell have been used for lithium alloy and graphene oxide battery studies [97, 113]. Briefly, the battery was comprised of cells symmetrically fabricated by two flat Li metal foils (7 mm × 7 mm × 0.75 mm) separated by a flat glass fiber and inserted into the Kel-F holder. An electrolyte, such as propylene carbonate, was incorporated and the entire system was glued/epoxy-sealed with a Kel-F cap containing a 1 mm hole in the center for the copper wires carrying the current [114]. The cell and glass spacers fit tightly inside the plastic holder, which is capped and glued shut prior to placement inside the probe and magnet. The design can be subsequently improved by removing the need to rely on glue to form the seal by utilizing O-rings. Further improvements come from stacking, but separating, electrodes and connecting them electrically in parallel to enhance the sensitivity of the spectroscopy. The use of O-rings will improve operating conditions and quality of the seal.

The most recent design of an *in situ* NMR battery cell was developed in Germany by Kayser *et al* [116]. The design incorporated carefully 3D printed components that enabled a rigid seal, reproducible cell compression, and long-run capabilities (tested up to 2400 h). The battery cell is placed on the bottom of a hallow plastic cell body. The body has a smaller hole which the battery covers wherein a contacting stick will consistently apply the same pressure to the bottom of the cell due to a change in diameter of the shaft and hole. A top piece slides into the bore of the cell body to contact the top of the cell. This also has a hole for a second contacting stick to similarly apply a consistent contact to the battery cell. The entire apparatus is sealed tight with nuts that compress bellowed cutting rings. This method has shown good sealing with a loss of just 1 bar of 15 after 1 d. Based on the material components used, the cell should be able to tolerate up to 120

°C and exhibit good chemical resistance over many years. The entire cell fits into a homemade saddle coil positioned with careful attention to the alignment within the magnetic field to ensure consistent and reproducible measurements [106, 117, 118]. Though still a new development, this cell paves the way in understanding the degradation pathways for batteries across hundreds of cycles due to its reliability and robustness.

Nowak *et al* have developed an *in situ* battery cell for liquid electrolyte measurements [119]. This device employs a cylindrical battery that rests atop the electrolyte measurement area, i.e. an extended compartment containing only liquid electrolytes intentionally placed inside the NMR detection coil. The authors report ^{1}H and ^{19}F measurements to monitor signals associated with fluoroethylene carbonate and fluoromethyl methyl carbonate during electrochemical cycling. Through these initial demonstrations, a detection limit of 200 μmol l^{-1} was determined for ^{1}H and ^{19}F in this cell.

3. *Ex situ* NMR techniques

While *in situ* techniques are certainly the pinnacle of representing a battery's operational condition, difficulties can arise in capturing the species of nuclei that are relatively more challenging to probe in terms of both sensitivity and linewidth. While ^{1}H, ^{7}Li, and in some cases ^{13}C are great candidates for time-resolved NMR spectroscopy, low sensitivity, low abundance, and quadrupolar nuclei strongly rely on magic angle spinning (MAS) and longer spectral acquisitions for a detailed and highly resolved picture of the sample's chemical state, especially when in the solid state. Battery applications employ an array of atoms that can be probed with NMR, including ^{1}H, ^{2}H, ^{6}Li, ^{7}Li, ^{13}C, ^{15}N, ^{17}O, ^{19}F, ^{25}Mg, ^{29}Si, ^{31}P, ^{51}V, ^{133}Cs, and others [39, 114, 120–126]. Many of these are either quadrupolar or low abundance nuclei.

While informative, the highly abundant and spin ½ nuclei do not always provide the clearest understanding of the chemical system. To compensate, less abundant or quadrupolar nuclei are often probed to investigate the detailed molecular environments in battery materials. Low abundance nuclei are a particular challenge for this relatively insensitive spectroscopic technique ^{17}O, for example, is a nucleus with natural abundance of only 0.038%. Moving to a high field can help promote a stronger oxygen signal through a more pronounced Zeeman interaction. However, more distinct advantages can come from employing a probe that allows for a larger sample volume since the detected signal is directly proportional to the number of spins in the coil. If isotopic enrichment is not practical, an increase in sample volume is generally the simplest way of boosting a signal to acquire detailed information about a chemical system. ^{17}O is also a quadrupolar nucleus, resulting in relatively broader lines. A number of interactions contribute to the resulting spectrum, as indicated by this summation of Hamiltonians:

$$H_{\mathrm{Int}} = H_{\mathrm{Z}} + H_{\mathrm{D}} + H_{\mathrm{CS}} + H_{\mathrm{K}} + H_{\mathrm{J}} + H_{\mathrm{P}} + H_{\mathrm{Q}}^{1} + H_{\mathrm{Q}}^{2} + H_{\mathrm{Q}}^{n} + \ldots$$

where the Zeeman (Z), dipolar (D), chemical shielding (CS), Knight shielding (K), spin-spin coupling (J), paramagnetic (P), and nth-order quadrupolar (Q) interactions can all play a role in the resulting NMR signal. Quadrupolar nuclei generally suffer from low symmetry and wider lines due to the quadrupolar interactions that arise from the anisotropyof the nucleus charge distribution with the electron field gradient. This quadrupolar effect can be partially reduced by employing more powerful magnetic fields. In cases where the quadrupolar nucleus also resides in a solid, which may be in the case of extracted SEI, more advanced techniques are required for high resolution spectroscopy. The advent of MAS has also had a dramatic impact on the interpretation of NMR spectra [127]. This technique allowed for solid samples to approach resolutions obtained with liquid samples by averaging out many of the interactions that impact line-width. Odd-ordered Quadrupolar Hamiltonians converge to zero when the sample is rotated at 54.74° with respect to the external magnetic field, leaving behind only the even-ordered quadrupolar terms and dramatically improving the signal to noise ratio of a spectrum. As outlined later, the strategies of employing larger sample volumes, higher magnetic field, and MAS have all been used to make experimental observations on natural abundance, quadrupolar and solid samples.

While highly abundant nuclei are relatively more studied due to the ease of acquisition, in some cases they are not the best suited for an application. Lithium-based batteries, in particular, have a large body of research where ^{7}Li and ^{6}Li NMR have been both utilized to gain insight on the system [113, 114, 128–131]. ^{7}Li is a spin 3/2 nucleus of 92.5% natural abundance, making its acquisition easy relative to ^{6}Li ($I = 1$, 7.5% nat. abundance). Further, ^{6}Li also suffers from low sensitivity due to its generally longer relaxation times; however, the quadrupole moment is smaller than that of ^{7}Li (~$2.4 \cdot 10^{-30}$ versus ~$4 \cdot 10^{-30}$ e m^2) and dipole-dipole interactions are also much weaker, allowing for higher spectral resolution and significantly enhanced structural information [132–134]. This can provide a direct benefit in situations in which two Li are near each other, a closer approximation of the isotropic chemical shift is desired, or the source of relaxation is not well-understood. For batteries, the relatively more challenging ^{6}Li might be a preferred technique if a variety of Li species are present and high spectral resolution is required to distinguish the signals. An additional advanced method for *ex situ* analysis of Li-based batteries includes pulsed field gradient (PFG) NMR, which has been employed to secure a firmer understanding of the role of temperature in the solvation structure of Li, Cs, and H species [135].

While significant strides have been made to push traditional battery system investigations towards *in situ* conditions, redox flow technology is primarily probed *ex situ* due to the difficulty of pumping steady streams of electrolytes along an interface while simultaneously detecting NMR-active species. These studies typically involve detailing the solubility and solvation structures of electrolytes in a given system to better understand solvent and ion interactions at different solute concentration levels to show the concomitant fluctuations of

contact-ion pair presence and solvent-solvent or solvent-ion interactions [136]. *Ex situ* NMR has been shown to reveal the key insights on the impact of functionalizing electrolyte components, such as ferrocene, towards enhancing the solubility to overcome performance barriers of non-aqueous electrolytes [137, 138]. Similarly, the rational design of electrolytes has been demonstrated for the vanadium redox system where the effects of chlorine have been discerned [139–142]. Indeed, NMR has become an important technique for characterizing the chemistry of electrolytes in redox flow battery systems [143–148]. This same strategy can be broadly applied to electrolyte systems of an array of battery classes. An example for understanding the solvation structure of electrolytes for Mg-based batteries will be detailed in section 5.5. It is important to mention that the NMR interpretation for many of these electrolyte systems is aided by computational modeling, which will be discussed in the subsequent section.

4. The role of computational modeling

While direct experimental observations are essential to a deep scientific understanding of a given battery process, computational approaches are gaining both popularity and importance for their predictive capabilities in chemical systems. Computational approaches become further important for relatively complicated spectroscopic studies where a given chemical system does not have a well-defined library of reference compounds that represent the chemical environments being probed. This might arise from unique environments only observed during a reactive process, or an entirely new material that has never before been probed. In these cases, it is often beneficial to complement NMR studies with computational simulations. As it applies to interpreting the NMR spectra related to batteries, two techniques serve as the primary aides in elucidating the signals observed; density functional theory (DFT) and molecular dynamics (MD).

DFT modeling is a computer-based method that uses quantum mechanics to describe the electronic structure of a many-body system. Functionals of the electron density are used to compute system properties. This method relies on exchange-correlation functional approximations that account for expectation differences when wave functions overlap and the influence of other electrons on a translating particle. This method allows for one to calculate the geometry and electron density of a system that can be used to compare to experimental observations. As it applies to battery systems, DFT can be used to better understand which structures show preferential formation during lithiation or model the effects of defects on cathodes [149]. It can also be used to calculate NMR parameters for comparison to collected spectra. A variety of methods can be used to accomplish this task [150]. A common method includes using the gauge-including atomic orbital (GIAO) approach [151–153]. In this, the shielding of a nucleus can be expressed as a second derivative of the total electronic energy referenced to an external magnetic field and magnetic moment of the nucleus. This method overcomes the unphysical 'gauge' complication of coordinate origin selection in the calculation and has been shown to deliver accurate results in comparing calculations to experimental results. Though many codes lack the ability to accommodate periodic NMR chemical shift calculations, the gauge-including projector augmented wave (GIPAW) method has enabled such computations [154]. This has reduced barriers to computations on systems that would typically require very large clusters to accurately model. Along with Quantum Espresso, PARATEC, and others, the CASTEP package, in particular, has been extensively used to apply this periodic method to battery research [155]. Much like experimental methods, the computational shielding calculations require the use of a reference compound, a library of which are available across the literature. All electron Slater basis sets tend to be used for these types of calculations since they describe core electrons more accurately than pseudo-potentials or Gaussians. Core electrons are generally free but the importance of accounting for these is not absolute given that sufficient shell electrons are accounted for [156]. This approach has been widely used to compare computational and experimental spectra ^{17}O or ^{25}Mg NMR in Li and Mg batteries [124, 157]. The DFT approach has also been used to understand electrolyte systems for which solvent effect codes, such as the conductor-like screening model (COSMO), or the inclusion of sufficient solvent shells are required [158]. This has been applied to better understand the solvent effects in a system [159, 160].

An additional challenge can present itself in applying DFT to heavier elements in batteries, such as for vanadium- or cesium-containing battery components, where the electrons of the *4d* orbitals begin to exhibit strong relativistic effects, requiring the use of the more computationally expensive (relative to the Schrödinger equation) Dirac equation. DFT-based total shielding calculations can be regarded as a sum of paramagnetic, diamagnetic, and spin–orbit coupling contributions. While relativistic effects may be accounted for without considering spin–orbit coupling, their applicability to accurate NMR calculations can be limited [161]. As such, NMR calculations considering relativistic effects often take advantage of the zeroth-order regular approximation (ZORA) [162, 163]. This method accounts for special relativity in heavier elements as electron speeds become more significant. ZORA is an excellent approximation to the fully relativistic Dirac equation, especially near the valance region. This improves the identification of species continuing heavier elements and secures greater confidence in the computational results. This computational method can be used to predict the NMR chemical shifts of structures that are likely to be present in the system. It should be noted that pure DFT calculations will not natively account for thermal effects on chemical shift since the calculations are based on 0 K. Effects such as chemical exchange between two species will require more robust methods to elucidate the structures present in the sample.

Still today, it can be difficult for DFT to accurately describe intermolecular interactions, especially dispersion forces where further perturbation terms may be necessary [164]. It is also challenging to model very large systems with hundreds of atoms to account for extended-order solvation schemes. To help determine the structure of a many-molecule

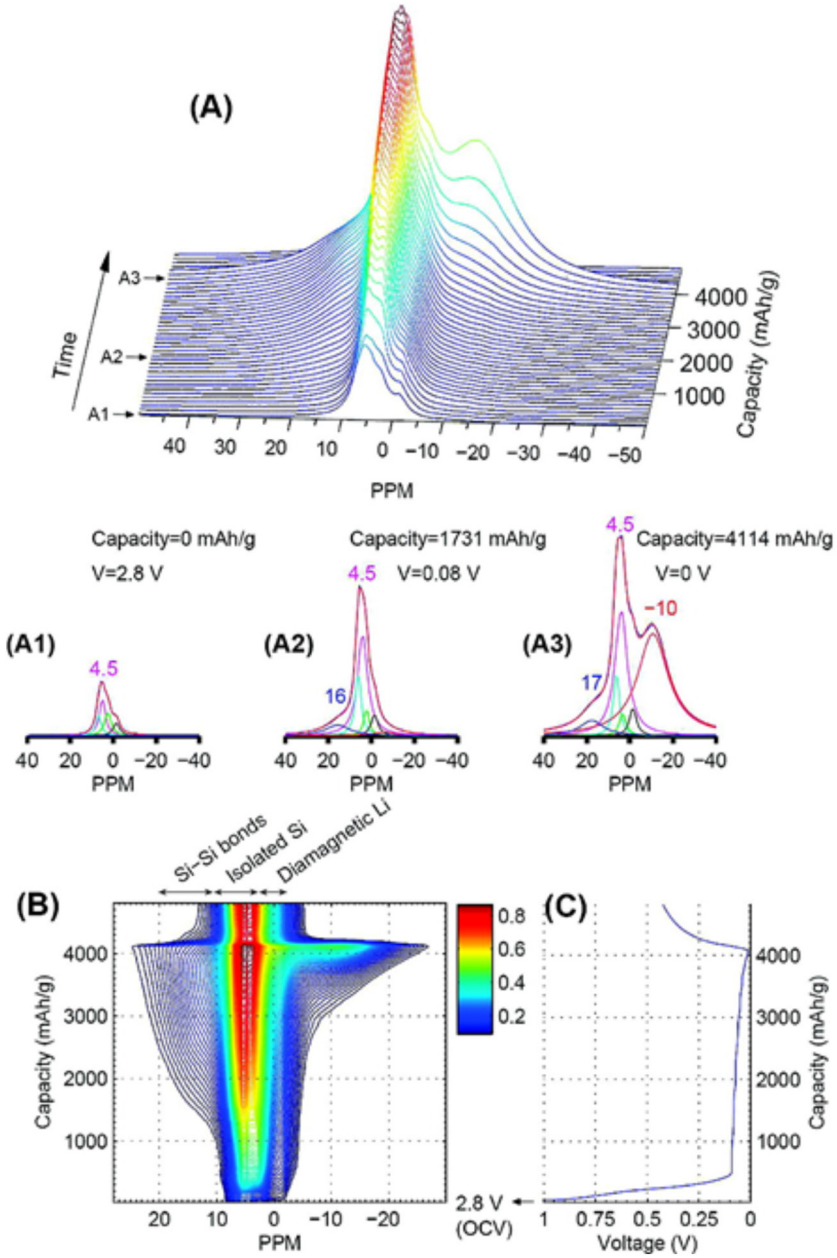

Figure 3. (A) Stacked and (B) contour plots of 7Li in situ NMR spectra of a Li/Si battery during the first discharge, with the corresponding electrochemical curve shown in part (C). Plots (A1)–(A3) show deconvoluted spectra at the specified voltages. Reprinted with permission from [115]. Copyright 2009 American Chemical Society.

system, MD simulations can be employed as a useful tool in understanding the nature of a battery system. Molecular Dynamics is a computational tool for understanding the motion of a many-bodied system based on Newton's equations of motions. *Ab initio* molecular dynamics simulations take this concept a step further and compute forces using Shrödinger's equations [165]. This powerful technique has been widely applied to study the SEI formation on Li–ion batteries [166–169]. It has also been used to understand the properties of electrolytes in batteries [170, 171]. Diffusion coefficients, for instance, can be approximated and compared to MRI values as well to better predict the state of the electrolyte during battery operation. MD can also be used for NMR calculations by taking the structures most likely to be present based on MD simulations and calculating the chemical shielding with DFT.

What may be a more robust approach would be to directly combine the strengths of the two methods to generate an aiMD-DFT, time-averaged picture of the chemical system. In this method, the MD simulation generates a series of snapshots from the trajectory for the molecules in the system. These configurations are used in DFT calculations to determine the NMR shielding tensors, which can be used to generate a weighted-average chemical shift of the configurations present for a given system. This combinatorial approach has been used extensively in solvated ionic platinum species, but can be useful in understanding complex electrolyte systems for battery applications [172–174].

5. Selections from recent research

The extraordinary importance of understanding the fundamental interactions in a given electrochemical cell has driven extensive research in the area with powerful *in situ* NMR investigations. Though numerous studies have been conducted that take advantage of this tool, the following important works demonstrate well the capabilities of these methods across a number of battery systems.

5.1. In situ NMR on Li-composite ion battery research

Composite anodes consisting of lithium and other metals (such as group IV Sn, Ge, Si) are attractive alternatives for traditional lithium anodes in Li–ion batteries. For instance, the use of Li–Sn composites have been investigated with NMR to demonstrate a 50% enhancement of lithium adsorption over carbon [175]. A brief review of *in situ* ^{7}Li NMR efforts in this area is available elsewhere that highlights the use of silicon, of interest due to its relatively high theoretical capacity [79]. Despite the interest in such materials, the precise structure of the lithiated species can be elusive to diffraction efforts due to the amorphous nature of the species. Lithium silicides, for example, have four reported stable crystalline phases, but electrochemical lithiation at room temperature favors an amorphous silicide. NMR has been applied to bridge the gap for these species by monitoring the transformation of lithium species during electrochemical cycling [115].

Silicon presents a popular material for composite anodes that has been investigated to better understand delithiation [131]. One prominent example of Li–Si composites is reproduced in figure 3. This illustrates the evolution of ^{7}Li species with time, whose signals strongly depend on their coordination environment with Si. Initially, four peaks are present between 0 and 8 ppm which relate to Li in the electrolyte, SEI on the positive and negative electrodes, and Li_XC. A broad peak ascribed to small silicon clusters begins to form around 18 ppm during the discharge process, which migrates to 14 ppm (A2). Additionally a resonance at 4.5 ppm (magenta) related to silicon clusters forms with discharging, indicating further breakage of the silicon linkages. The peak that forms in the later stages of discharge at −10 ppm arises from overlithiated, crystalline $Li_{15}Si_4$, which was not observed *ex situ*. The use of NMR helped solidify the understanding of Li–Si systems, explaining the nature of species present under reaction conditions and showing the reactivity of amorphous lithium silicides. Additionally, the authors discovered that excess-Li could facilitate self-discharge at low voltages, resulting in a loss of capacity for Si batteries.

Balancing the anode's high energy densities (992, 1623, and 4200 mAh g^{-1} for Sn, Ge and Si respectively) with excellent substrate lithium diffusivity and electrical conductivity places Li–Ge as an attractive option [176–178]. NMR has also been used to better understand strategies for stabilizing the structure of this composite. For instance, conventional methods of incorporating the group IV metals result in poor capacity retention across cycling. This effect stems from the drastic volume changes during the lithiation and delithiation process coupled with unstable formation of the SEI film. However, embedding Ge on a conductive scaffold can assist in the minimization of the detrimental volume fluctuations; however, inhomogeneity of metal deposition still negatively impacts the retention of energy storage capacity [179, 180]. To mitigate the effect, core–shell structures have been employed that show enhanced resistivity towards storage degradation [181, 182]. Despite these enhancements, the mechanisms by which Ge core-shells impact Li cycling were unclear, complicating performance optimization. Tang *et al* employed Ge nanorodes encapsulated by bamboo-type multiwall carbon nanotubes (Ge@CNT) for a Ge–Li planar half-cell battery and *in situ* NMR to better describe the roles of Ge in the Li–Ge battery [97].

Figure 4 shows the *in situ* ^{7}Li NMR results obtained during the first two charging cycles of a Ge@CNT Li–Ge battery half-cell, plotted as a function of cell capacity. They observed four ^{7}Li resonance lines centered at 24, 13, 10, and −24 ppm which were monitored together with the ^{7}Li signals of the electrolyte and SEI (0 ppm). From a detailed analysis of the collected data, supplemented with XRD, TEM, and STEM, it was concluded that the significantly shielded signal at −24 ppm could be attributed to an overlithiated $Li_{15+\Theta}Ge_4$ phase that was only present during the electrical contact. This phase was uniquely identifiable by NMR (not XRD or TEM) under reaction conditions. The absence of this overlithiated phase promoted the formation of a broad signal downfield that was attributed to a more amorphous Ge phase that may enhance the lithiation/delithiation rate. The remaining peaks could be assigned likewise by the properties exhibited during the various experiments (see table 2). They showed much greater stability towards a lack of electrical contact.

This study enabled key understandings surrounding the Li–Ge battery system, in particular, the reaction pathway during electrochemical cycling. The *in situ* ^{7}Li NMR studies revealed that the reversibility of lithiation in Ge@CNT is mediated by coexisting amorphous and crystalline phases present in the battery. It also enabled a deep understanding of the system's electrically-driven metastable $Li_{15+\Theta}Ge_4$ phase that was only possible during electrical contact on the carbon walls that encapsulated the Ge. Using a combination of the techniques, the authors were able to propose a reaction pathway that accounts for all spectroscopic and microscopic observations as well as phase transitions available during cycling:

$$\mathrm{Ge}(c) \rightarrow \mathrm{Li}_{2.26}\mathrm{Ge}(a) \rightarrow \mathrm{Li}_{15}\mathrm{Ge}_4(c) + \mathrm{Li}_{3.5}\mathrm{Ge}(a)$$
$$\rightarrow \mathrm{Li}_{15+\theta}\mathrm{Ge}_{4,\mathrm{metastable}}\,(c) + \mathrm{Li}_{3.5}\mathrm{Ge}_{\mathrm{metastable}}(a)$$

where (c) indicates a crystalline phase and (a) is the designation for amorphous. This model well-reflects the progression of phases identified with the *in situ* NMR to describe the lithiation process during electrochemical cycling. It was speculated that the enhanced capacity from such carbon-encapsulated Ge was related to the formation of these metastable states during electrical contact. Such observations are unique to *in situ* NMR and promote a deeper understanding of composite battery systems. A number of additional *in situ* NMR studies have focused on composite anode and cathode materials

Table 2. Summary of *in situ* ^{7}Li NMR Observations. Reprinted with permission from [97]. Copyright 2015 American Chemical Society.

Resonance index	Assigned phase	Chemical shift/ppm	Potential/capacity∗	Crystal property	Observed by
R1	$Li_{2.25}Ge$	24	0.17/839	Amorphous (*in situ* XRD	NMR (*in situ* ^{7}Li)
R2	$Li_{3.5}Ge$	13	0.14/1086	[183] and TEM)	NMR (*in situ* ^{7}Li)
R3	$Li_{15}Ge_4$	10	0.11/1325	Crystalline phase (*in situ* XRD [183] and TEM)	NMR (*in situ* ^{7}Li), *in situ* XRD [183]
R4	$Li_{15+\Theta}Ge_4$	−24	0.005/1653	Over-lithiated	NMR (*in situ* ^{7}Li)

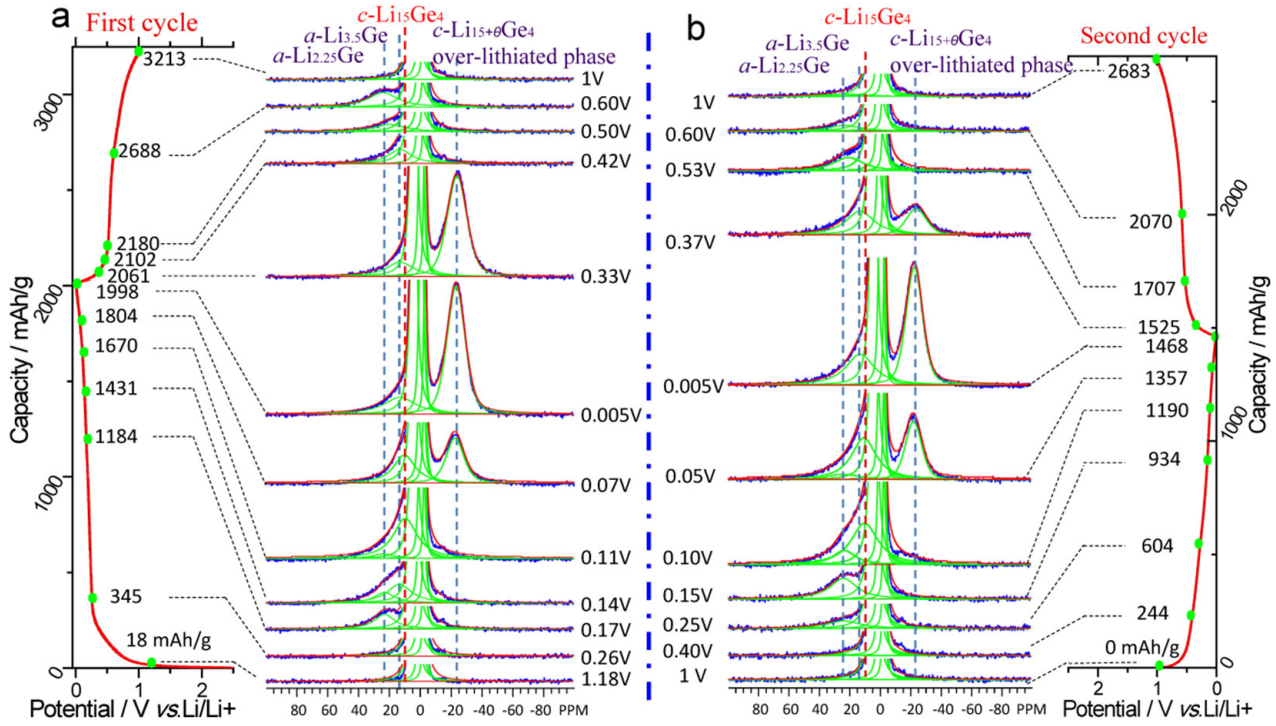

Figure 4. Selected *in situ* ^{7}Li NMR spectra of the Ge@CNT composite during the first (a) and second (b) charge/discharge cycles. Reprinted with permission from [97]. Copyright 2015 American Chemical Society.

using ^{6}Li and ^{7}Li, to provide a detailed understanding of the microstructure formation of Li dendrites, ion hopping, and phase transitions with a variety of electrode materials [115, 184–186].

5.2. *In situ* NMR on Li–S battery research

Lithium-sulfur electrochemical cells are battery systems that hold great potential advantages over conventional Li–ion batteries due to improvements in specific energy (~2500 Wh kg^{-1}) and low-cost production options [187–189]. In these systems, soluble lithium polysulfide species are formed as intermediates important to the energy transfer chemistry; however, dissolved species may also lead to poor electrochemical performance and failure. Though a number of *in situ* methods have highlighted the importance of the reaction in system understanding, they failed to provide a quantitative look at the evolution of the present species, instead focusing on identification of discrete sulfur or lithium polysulfide compounds [49, 53]. *In situ* NMR has the distinct advantage of simultaneously identifying and quantifying all NMR-active species during the charge, discharge, and standby periods of battery cycling. This concept was applied to the Li–S system using the cylindrical microbattery *in situ* NMR cell pictured in figure 5(A) [96]. A lithium metal anode (100 μm thick in blue) was separated from the cathode with Celgard 2500 of thickness 25 μm (red). The sulfur-based cathode film (around 175 μm thick) was laminated onto an aluminum mesh (green) where binding utilized polytetrafluoroethylene. In this system, the transient nature of Li species was monitored over several charge/discharge cycles to capture the microstructural evolution of the species in the various components of the battery.

The resulting ^{7}Li spectra were plotted as a function of time, where each spectrum was collected in just 4 minutes (see figure 5(B)). Representative spectra were selected and deconvoluted (figure 5(C)) to identify eight unique lithium species that could be identified with high confidence due to a more solid understanding of the evolution of these during the charge/discharge process (figure 5(D)) not available during *ex situ* measurement [64]. Though *ex situ* measurement of each the separator, cathode, and anode could be compared, a more clear assignment of these peaks arose based on the observed chemical shift, known species previously identified at a given voltage, and the line intensity change as the experiment

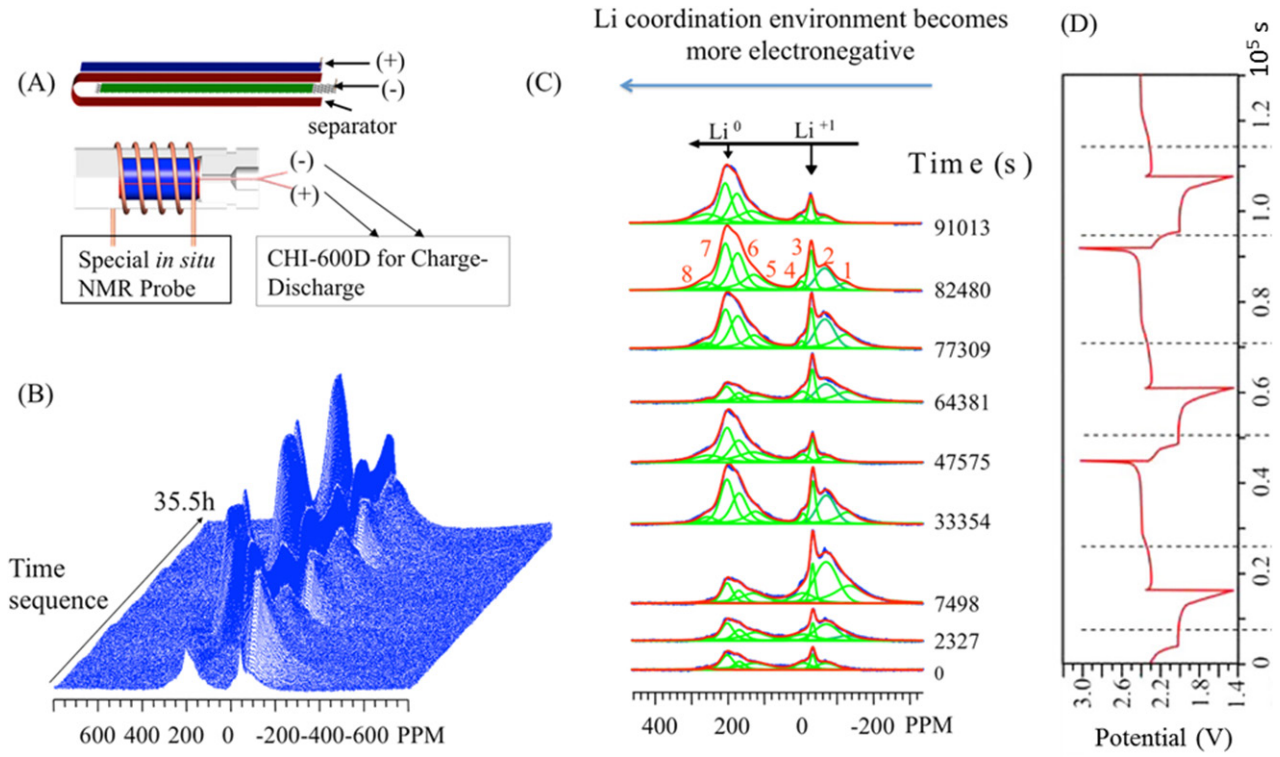

Figure 5. *In situ* NMR data collected for a Li–S battery system showing (A) schematic of the cylindrical microbattery, fitted into the *in situ* NMR probe, (B) stacked-plot data of 500 *in situ* ^{7}Li NMR spectra in the functioning Li–S battery cell during the charge/discharge cycle, (C) major peaks of interest extracted at selected times by fitting the spectra, and (D) the voltage profile of the Li–S cell used in the NMR measurements. Peaks are labeled as (1,2) soluble long-chain polysulfides, (3,4) insoluble Li_2S_X on the electrodes, (5–7) quasi-metallic, porous lithium, and (8) dendritic Li. Reprinted with permission from [96]. Copyright 2015 American Chemical Society.

progressed. This first *in situ* study using the cylindrical micro Li–S battery demonstrated that the reaction pathways were composed of mixed species in a complex environment instead of discrete step-by-step reactions.

For example, peak 1 at −128 ppm was identified as a soluble long-chain polysulfide since S_8 is expected to reduce to this species at around 2.3 V. This was confirmed by the maximum intensity arising during the 2.1 V charge plateau, a minimum during the end of the discharge when insoluble Li_2S_2/Li_2S dominate, and on the basis of chemical shift value. This species was shown to directly and rapidly convert to long-chain polysulfides instead of relying on the accumulation of additional LiS_4 species. Further, this peak and its analog at −100 ppm were not visible except under *in situ* conditions and is attributed to Li^+ interacting with long-chain polysulfides as well as sulfide radicals. The second peak (−71 ppm) was similarly associated with soluble long-chain polysulfides such as Li_2S_8 or Li_2S_6. The remaining peaks, high field peaks 3 (−34 ppm) and 4 (−7 ppm), were described as insoluble Li_2S_2 or Li_2S on the lithium electrode.

Peaks 5, 6, and 7 were challenging to clearly identify, but on the basis of Li metal shifts near 250 ppm (Knight Shift from electrons in the conduction band) these are tentatively assigned as quasi-metallic, porous lithium species. These species also follow the opposite trend as the polysulfide signals. Peak 5 reaches a maximum intensity as the cell is fully charged whereas peaks 6–8 reached their maximum at 50% charge and declined to a local minimum at full charge. This suggests the growth of the porous lithium species in the deposition process and the concomitant reduction of the signals for peaks 6–8. These peaks were further found to relate to Li involved in creating the SEI. In particular, signal 8 (254 ppm) is assigned as a dendritic or thin mossy Li environments on the anode material.

In situ NMR also supports the hypothesis that the reaction pathways during charge and discharge differ due to the evolution of species observed and the differing lengths of the two plateaus of the charge-discharge curve.

This important *in situ* work was able to clarify the evolution of species involved in SEI layer formation as well as anode surface roughening and dendritic nucleation. Unique polysulfide environments became apparent during the charge and discharge process that cannot be captured by *ex situ* investigation. Confirmation of transient free radical presence offers key insights into the degradation of battery performance. Observations like those collected for this Li–S battery study offer molecular-level insights that are crucial to the accelerated development of the technology. A number of *ex situ* NMR studies employing ^{7}Li and ^{1}H NMR have continued to investigate the key uncertainties surrounding this technology to compliment *in situ* studies such as See *et al*'s attempts to better describe the Li–S phase diagram [64, 190–192].

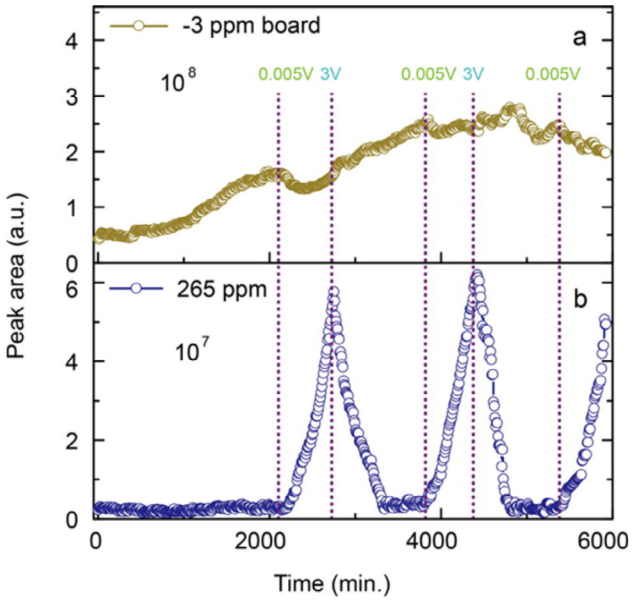

Figure 6. *In situ* NMR peak area evolution of the (a) −3 ppm broad and (b) 265 ppm peaks during the charge and discharge cycles. Reprinted with permission from [113]. Copyright 2016 American Chemical Society.

5.3. In situ NMR on Li–ion battery research

Numerous highly respectable efforts have employed *in situ* NMR to detail the chemical transformations occurring, such as extraction, insertion, and dendritic growth [81, 111, 118, 193]. For instance, the effect of carbon coating graphite for use as an anode was shown to have two sites for lithium; the graphite core and soft-carbon shell for intercalation and storage, respectively. The ^{7}Li NMR showed the the relative abundance of the two sites was well correlated to the extent of coating, explaining the decrease in irreversible capacity and increase in coulombic efficiency [194]. Recently, lithium-ion battery technology utilizing reduced graphene oxide (rGO) has attracted great interest as a high capacity alternative to graphite anodes due to its high surface area and conductivity [195–200]. However, the lithiation mechanism for rGO was poorly understood relative to that of graphite-based cells, where differences in the mechanisms are evidenced by its increased capacity over graphite (600–1000 mA h g^{-1} versus 372 mA h g^{-1}). To better understand the evolution of the SEI layer on rGO, *in situ* studies employing Raman spectroscopy and an NMR battery cell were conducted to monitor the temporal evolution of the G-band and ^{7}Li signal during the charge and discharge cycle [113].

For both the graphite and rGO anodes, the *in situ* Raman shows a decrease in the G-band at ~1582 cm^{-1} as the battery was discharged. This was ascribed to a resonance loss by the intercalation of Li, increasing the homogeneity of the sample. In the case of graphite, a 9 cm^{-1} upshift is observed during cathodic polarization due to the donated electrons to the carbon. Contrasting the graphite's loss of G-band below 0.2 V, the rGO sees this disappearance around 0.3 V. To provide additional insight, Tang *et al* used *in situ* ^{7}Li NMR to monitor the specific chemical environments of lithium species. A number of distinct lithium species were detected in the *in situ* experiments. Upfield, a broad peak at −3 ppm and a few small, sharp peaks around 0 ppm were present. The sharp peaks at 0 are indicative of solvated lithium species while the broad signal is attributed to a combination of lithium intercalated into the rGO lattice and adsorbed on the surface functional groups present on rGO [201, 202]. Downfield, three peaks at 244, 250, and 265 ppm are present that relate to the Li–metal electrode. The peaks at 244 and 250 were attributed to a 10 μm skin layer on the Li–metal surface while the 265 ppm peak was assigned to the Li–metal fibers perpendicular to the metal surface [73]. Notable changes were observed for the broad peak at −3 ppm and the peak at 265 ppm that provided insight on the electrochemical process. As seen in figure 6, the evolution of the various chemical species present could be tracked along the charge/discharge cycles.

The −3 ppm peak intensity evolution shows the clear enhancement of signal over the course of the experiment, approximately quadrupling in intensity by the end of the third charge cycle. The intensity of the intercalated/adsorbed lithium species is shown to increase over the discharge periods and reduce in abundance as the cell is charged. Conversely, the Li–metal fibers (256 ppm) remain nearly absent until charging initiates, reaching a maximum at the end of the first charging cycle. As discharging is initiated, the peak intensity falls as lithium ions are peeled from the surface of the metal. The concurrent and opposite behaviors during cycling demonstrate well the fate of Li species in electrochemical cycling. Tang *et al* made the interesting observation that only a small portion of the −3 ppm species is participating in the cycling, suggesting that a majority of the lithium that had moved to rGO were inactive and participating in the formation of the SEI with the surface functional groups (–H, –OH,–COOH, –C=O, etc). The second charge/discharge cycle demonstrated an increased Li–metal species compared to the first cycle, showing a relative stabilization of the SEI after the first cycle. This observation was confirmed by the third cycle, which may serve to explain the high capacity of rGO during the first cycle and reliability during subsequent cycles, quantified by the area of the Li–metal peak.

Combined with the CV and additional NMR experiments, it was concluded that the primary difference between rGO and graphite was the preference of rGO to intercalate Li via surface adsorption instead of the conventional graphite mechanism. The passive SEI in rGO was formed during the first electrochemical cycle and was stabilized afterward. Approximately 36% of the intercalated Li^+ was recycled during the first cycle. While the detailed structure of Li in the SEI could not be resolved, the differentiation between Li^+ in the SEI and the counterpart on the rGO is directly visible as a function of time and electrochemical cycling. This study highlights the power of NMR to observe quantitative, real-time descriptions of battery constituents under unique chemical environments. Additional NMR studies related to this topic have made a variety of contributions to our understanding of Li–ion batteries [79, 111, 118]. Important and decisive observations, such as the mass transport limitations present in high-power Li–ion

powered vehicle applications, are greatly assisted by these *in situ* NMR methods [203].

5.4. In situ and ex situ high-field NMR studies of Li–metal batteries

Li–metal batteries offer a high energy density option relative to Li–ion battery technology, but also pose a number of challenges in the safe recharging of the cell. The origin of the rechargeable Li–metal battery research finds itself in the 1970s [204]. Of interest as an anode due to its low electrochemical potential (−3.04 V with respect to hydrogen electrode), low material density (0.534 g cm^{-3}), and high theoretical capacity (3860 mA h g^{-1}), limited success was realized due to poor columbic efficiency and dendritic growth of Li during charging cycles [205, 206]. The cycling stability of Li strongly depends on the interactions with the electrolyte, in particular where organic solvents render Li unstable and promote the formation of these microstructures. It has been identified that addition of certain species to the electrolyte forms a uniform, solid SEI or alloy with Li during deposition that can suppress dendrite formation and thus increase the cycling life [207–211]. For example, one approach to suppress dendritic growth is based on a self-healing electrostatic shield where low concentrations of Cs^+ or Rb^- in the base electrolyte form a positively charged electrostatic shield around the nucleation points (Li tips). This forces deposition to adjacent regions to reduce dendrite formation [212]. Microscopy even identified a dendrite-free Li film, suggesting the presence of synergistic effects between the Cs^+ and SEI [213]. Previous *in situ* NMR investigations on Li batteries have quantitatively tracked the real time dynamics under working conditions [80, 101, 105]. One study even highlighted the deposition of dendritic Li on the Li electrode during cycling [73]. This study, however, found a wide range of possible shifts (242–272 ppm) for a given species depending on its orientation with respect to the magnetic field. To amplify potential important signals in this region, the bulk magnetic susceptibility effect was clarified by employing planar symmetric Li metal cells measured as a function of the normal direction relative to the magnetic field for the study of the Li–metal battery system with and without the Cs^+ additive [114].

The study highlighted the importance of Cs^+ in the formation of well-aligned Li nanorods and reversibility of the Li electrode. Though a number of studies readily utilize ^{7}Li NMR, this one also incorporated ^{133}Cs NMR technics to probe the dynamics of Cs^+ in the battery. The *in situ* ^{133}Cs NMR clearly showed the migration of Cs^+ to the Li electrode to form a positively charged electrostatic shield during the charging process, evidenced by a significantly broadened signal compared to the narrow signal of a solvated Cs species. It was found that the Cs intensity was retained and reversibly solvated at the other end of the electrochemical cycle. The results also indicated a much larger fraction of the Li taking part in the cycling process when the additive was present. The rods generated in the absence of Cs tended to be much thicker and lead to a large fraction of inactive lithium species.

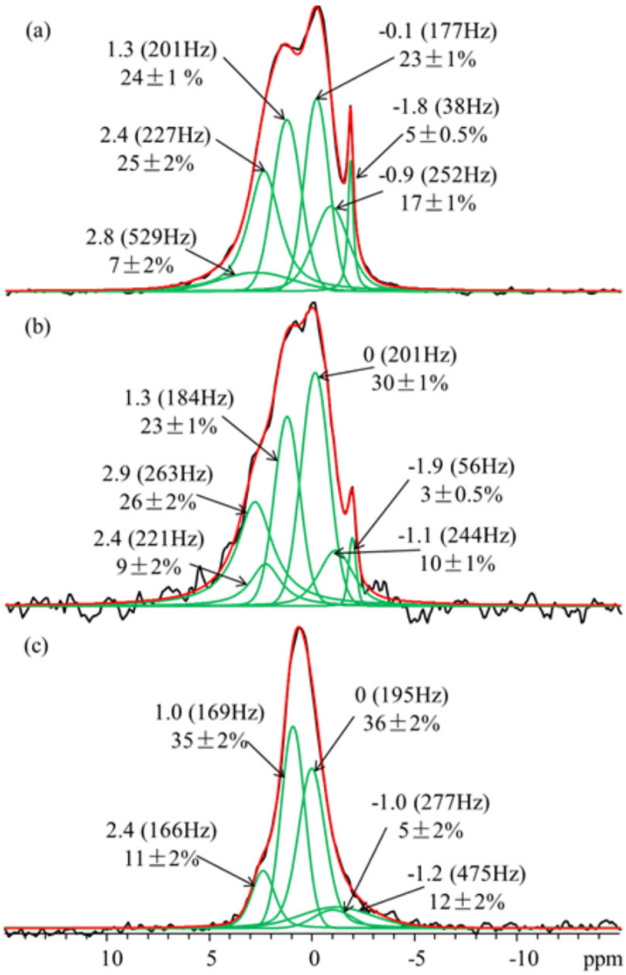

Figure 7. The expanded spectral region plots between −15 and 15 ppm and the deconvolutions of the ^{6}Li MAS NMR spectra obtained at high field of 850 MHz spectrometer for the SEIs harvested from CulLi batteries with (a) 4 M LiFSI-DME, (b) 1 M LiFSI-DME, and (c) 3 M LiTFSI-DME as electrolyte. Peaks are assigned to Li_2O (2.8 ppm), Li_2S (2.4 ppm), LiOH (1.3 ppm), Li_2O_2 (−0.1 ppm), LiF (−0.9 ppm), and LiFSI (−1.8 ppm). Reprinted with permission from [216]. Copyright 2017 American Chemical Society.

In addition to *in situ* Li–metal investigation, NMR has provided unique insights with *ex situ* techniques, particularly for low-sensitivity nuclei. The formation of new SEI layers as the battery was cycled that trap metallic lithium in the passivation film poses a potential safety hazard, making the SEI a target for detailed investigation [214, 215]. One notable example of *ex situ* NMR took advantage of ^{1}H, ^{6}Li, ^{13}C, and ^{19}F NMR to study the SEI formed on the copper electrode. Wan *et al* employed the unique advantages of ^{6}Li NMR over ^{7}Li NMR to obtain a higher spectral resolution in the recovered SEI of a number of CulLi cells [216].

This work analyzed the SEI extracted from CulLi cells using two different concentrations of lithium bis(fluorosulfonyl)imide (LiFSI) in 1,2-dimethoxyethane (DME) as electrolytes (LiFSI-DME samples), including one lithium bis(trifluoromethanesulfonyl)imide (LiTFSI)-DME sample. The cells were cycled such that a 1 h deposition time was utilized to a capacity of 1.0 mA h cm^{-2} and

the stripping was controlled to an upper cutoff voltage of 0.5 V versus Li/Li^+. These cells were cycled 200 times prior to SEI extraction, preparation, and loading into a sealed 3.2 mm MAS rotor for *ex situ* ^{6}Li MAS NMR measurement. The authors were able to identify a number of lithium species using high-field ^{6}Li NMR spectroscopy. Across all samples investigated, metallic Li (264 ppm) was present that can stem from dead Li and broken dendrites that failed to cycle during the final delithiation stage. Relatively more metallic lithium is present in the least concentrated electrolyte (i.e. the 1 M LiFSI-DME), but fewer lithiated species can be observed compared to the other two concentrations, showing the clear impact of solution concentration on lithium species. By employing reference compounds and taking advantage of the higher spectral resolution afforded by ^{6}Li NMR over ^{7}Li NMR, six additional Li species were identified in the SEI of these cells: LiFSI, LiF, Li_2O_2, Li_2S, and Li_2O. Fluorine-containing compounds were verified by ^{19}F MAS NMR due to the highly sensitive nature of these signals to the chemical environment of F. ^{1}H and ^{13}C MAS NMR were also used to rule out potential Li species.

The spectra from the 15 to −15 ppm region can be viewed in figure 7. The 4M LiFSI-DME sample (figure 7(a)) contained Li_2O (2.8 ppm), Li_2S (2.4 ppm), LiOH (1.3 ppm), Li_2O_2 (−0.1 ppm), LiF (−0.9 ppm), and LiFSI (−1.8 ppm). The 1M LiFSI-DME sample (figure 7(b)) could be deconvoluted with peak that aligned well to those of the 4M LiFSI-DME sample, except that no ^{19}F peak was present, suggesting that the −1.1 ppm peak is a different species from LiF; a number of options were proposed in the full text. Figure 7(c) shows the spectrum for the 3M LiTFSI-DME sample, which showed similar features as the 4M LiFSI-DME sample, but without Li_2O and the presence of LiTFSI instead of LiFSI. Higher concentrations of LiFSI/DME resulted in an overall thicker SEI with fewer dead Li–metal species. This trend was observable across the three samples and explained the enhanced electrochemical performance at high LiFSI concentrations in DME. While this is one example of *ex situ* NMR assisting in the characterization of how Li–metal battery formulation impacts the SEI, numerous others are available in the literature [132, 217].

5.5. Ex situ NMR studies of solvation structures

A key component to battery systems are the electrolytes responsible for energy transfer. Their observation by NMR can lead to a detailed understanding of the electronic environment and thus their molecular arrangements. While a number of electrolyte components have been mentioned previously, less abundant and recorded nuclei can provide valuable insight. The challenge associated with this, however, is the low concentration and abundance of species, such as ^{17}O in nonaqueous carbonate electrolytes [123]. In this, Bogle *et al* were the first to employ natural abundance ^{17}O NMR measurements to such electrolyte systems, demonstrating a maximum of six ethylene carbonate molecules in the Li^+ solvation sheath accompanied by dimethyl carbonate.

Often, a confident assignment of signals for such electrolyte systems is hindered by the structural interpretation of the lines observed. Without supporting experimental data for similar structures and trends, it can be very challenging to describe the exact coordination of molecules in the electrolyte, necessitating the application of theoretical calculations. Our group's recent work highlights the power of combining NMR spectroscopy with high-level theoretical calculations for a deeper understanding of battery-related electrolyte systems [218]. For such applications, our group often utilizes a specialized large sample volume probe established for ultra-high field (850–900 MHz) was employed [74, 219, 220]. The probe permitted up to 2 ml in sample volume, allowing for natural abundance detection of Mg at concentrations as low as 10 mM within just a couple hours of sampling ($S/N \sim 60$). The first reported application of the probe with respect to battery technology employed the technology for analyzing the natural abundance ^{17}O signals in lithium-based electrolytes [74]. In this work, Deng *et al* collected natural abundance ^{17}O spectra of Li-bis(trifluoromethane sulfonyl) imide (LiTFSI) at concentrations around 20 mM to elucidate the solvation structures of LiTFSI in various solvents and mixtures of the solvents. Accompanying the high-sensitivity NMR studies, DFT-based models of the solvation structures helped determine the coordination and exchange structures of Li^+ in the solvents at various concentrations in an attempt to understand the barriers a given electrolyte might encounter during battery operation. A more recent study highlights this principle by combining electrochemical evaluation, high-field natural abundance ^{25}Mg NMR, classical molecular dynamics simulations, and DFT-based chemical shift calculations to understand the solvation structure for Mg-based battery technology [83].

Due to a rise in evidence suggesting that the solvation structure of a liquid electrolyte has a dramatic impact on the electrochemical performance of batteries, a detailed investigation of Mg-battery electrolytes was conducted by dissolving magnesium borohydride [$Mg(BH_4)_2$] and $Mg(TFSI)_2$ in diglyme (DGM) [160, 221, 222]. The rational development of improved electrolytes requires an understanding of how the components interact with each other, and as such, how the solvation structure plays an important role in the resulting properties. Mg batteries offer an attractive alternative to Li–ion designs due to the potential to triple the volumetric energy density [223]. However, a number of challenges exist in utilizing Mg as an energy carrier. One prominent drawback is the employment of an electrolyte capable of operating across a wide electrochemical window while simultaneously allowing reversible plating/stripping of Mg [30]. Since Mg forms an ionically blocking layer when exposed to oxygen, inhibition of deposition is a difficult challenge for Mg-based battery systems to overcome, driving the need for a designer electrolyte system to either prevent or reduce this interaction of the SEI [224, 225]. Halo, organo, and organo-halo salts are known to allow reversible Mg deposition, but they have limited anodic stability and conductivity [226]. A more conductive salt such as $Mg(TFSI)_2$ suffers from difficulties in the reversible stripping process. To better understand how continued improvements to these electrolytes can be realized, a

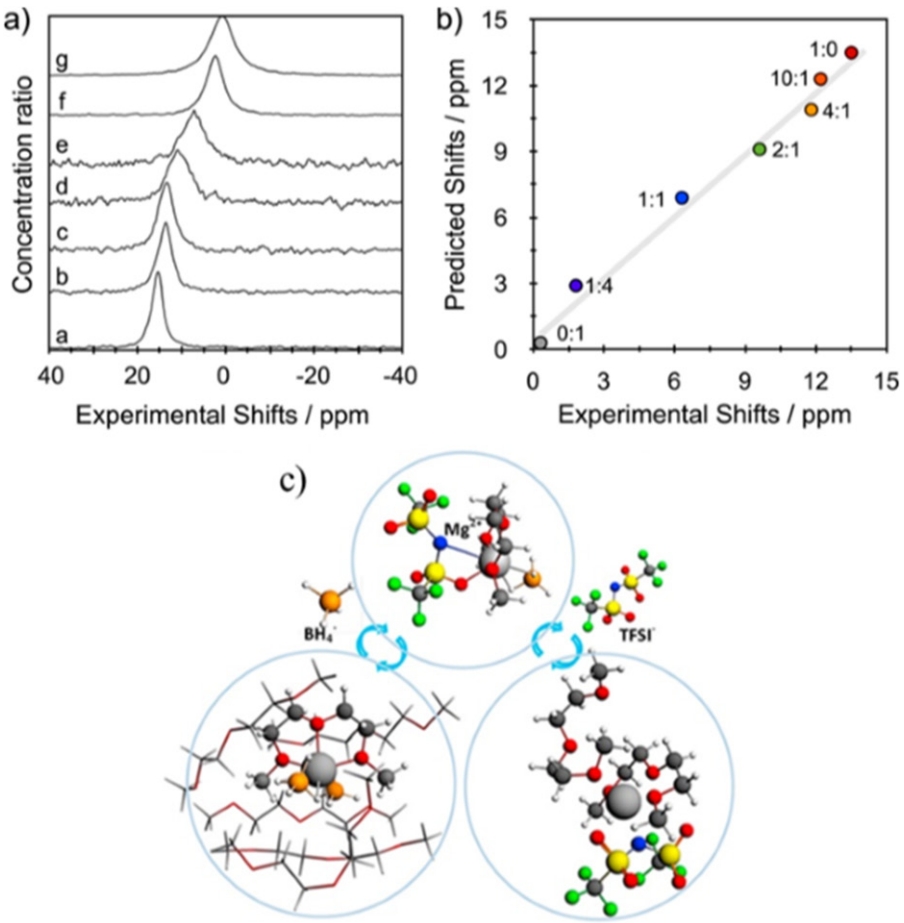

Figure 8. (a) ^{25}Mg NMR spectra of $Mg(BH_4)_2$ and $Mg(TFSI)_2$ dissolved in DGM with different concentrations of ($Mg(BH_4)_2$:$Mg(TFSI)_2$). (a) 0.01 M:0 M; (b) 0.01 M:0.001 M; (c) 0.01 M:0.0025 M; (d) 0.01 M:0.005 M; (e) 0.01 M:0.01 M; (f) 0.01 M:0.04 M; (g) 0 M:0.4 M. (b) Correlation between the predicted chemical shifts and experimental results. (c) Proposed solvation structure rearrangement mechanism. The labels on the points are the molar ratios of $Mg(BH_4)_2$:$Mg(TFSI)_2$. Reprinted from [83], Copyright 2018, with permission from Elsevier.

detailed assessment of the structural aspects is required to understand the solvation environments.

Our team has investigated the solvation structures of Mg^{2+} with varying concentrations and combinations of $TFSI^-$ and BH_4^- mixtures using a combined experimental and theoretical approach, chiefly employing the large sample volume probe for natural abundance ^{25}Mg NMR measurements combined with quantum chemistry calculations and molecular dynamics simulations to relate the electrolyte structures to their electrochemical performance [83]. The experimental results as well as the predicted shift accounting for molecular exchange are presented in figure 8. Figure 8(a) shows the experimental results of the natural abundance ^{25}Mg experiments from pure 0.01 M $Mg(BH_4)_2$ (a), mixed $Mg(BH_4)_2$ and $Mg(TFSI)_2$ electrolytes (b)–(f) to pure 0.4 M $Mg(TFSI)_2$ (g). The observed experimental shifts of the various counter-ion concentration ratios agree well with those predicted based on the molecular exchange principle:

$$\delta_m = \frac{c_1}{c_1 + c_2}\delta_1 + \frac{c_2}{c_1 + c_2}\delta_2$$

where c_i is the concentration of a given species and δ_i is the chemical shift of the pure, dilute Mg salt.

To interpret the results, molecular dynamics simulations were employed to predict likely structures of the salts at various concentrations. Analyzing the residence time and radial distribution of the molecules in the simulation provided a clearer picture of which structures were most likely and to which electrolyte components Mg shared coordination. The resulting structures were then used as models for DFT-based chemical shift calculations. This approach assisted in interpreting the NMR data to provide clear evidence on the solvation structures of the electrolytes due to the agreement between experimental and computational data.

For the pure $Mg(BH_4)_2$ salt dissolved in DGM, the first solvation shell contains two BH_4^- anions and one DGM as a tridentate chelating the Mg^{2+}, the second shell has 5–6 DGMs. The $Mg(TFSI)_2$ dissolved in DGM appears to take a first solvation shell containing one DGM as a tridentate ligand and a second as a monodentate ligand. A single $TFSI^-$ donates an oxygen and nitrogen atom to the Mg^{2+} cation. The second solvation shell contains ~4 DGM molecules. When the two salts are mixed, a fast exchange between the two pure component structures was discovered that proceeds through a third, intermediate structure containing one of each $BH4^-$, $TFSI^-$, and DGM in the first solvation shell and 5 DGMs in

the second shell. This intermediate structure was classified by molecular dynamics and accurately explains the observed shifts at high salt concentrations. The efficiency of the electrochemical performance was maximized at a $BH4^-$:$TFSI^-$ ratio of 1:4 and was attributed to the enhanced molecular dynamics and improved stability of the TFSI identified by the combined NMR and computational approaches. This work provides a clear demonstration of the power of NMR in characterizing the effect of the electrolyte solvation structure on electrochemical performance.

Combined computational and NMR efforts have also improved scientific understanding of electrolyte mixtures in redox-flow batteries. Investigations of electrolyte stability led to the development of a mixed-acid system with a dramatic increase in energy density and stability over conventional vanadium redox-flow batteries, for which NMR and theoretical evidence were combined to suggest the effect could be attributed to improved anion selection for the ligand exchange process [139, 140]. Similar concepts were applied to lithium-based redox-flow systems. Comprehensive NMR and DFT analysis was used to design and characterize an ionic-derivatized ferrocene to be the active redox species in the electrolyte. The enhanced dynamic interactions between solvent and electrolyte led to increased solubility that improved battery performance. Characterization identified that the Li-graphite anode prevented dendritic growth and SEI instability to promote stability over many charge-discharge cycles [227]. Indeed, the combination of NMR with DFT calculations of the chemical shift has deepened the pool of knowledge relating to electrolyte structures, but the dynamics of these processes are important too. Briefly, the role of NMR and MD calculations in elucidating battery science will be mentioned.

Since solvation structures are in constant motion and chemical species in electrolytes are diffusing, pulse-field gradient (PFG) approaches have also been employed to elucidate the solvation structure and dynamics [228, 229]. This technique has been used to show the strong relationship between cationic transference number and diffusivity [230]. Robust efforts to predict specific diffusion constants have also been proposed based on extensive NMR efforts [231]. Due to the empirical nature of these models, a more theoretical approach could provide a deeper understanding of diffusion in electrolyte systems. To support measurements of structure and diffusion, computational MD predictions of the diffusion constants can be well-matched with experimental values [232]. In this way, computational efforts that are not DFT-based have also played an important role in characterizing electrolyte systems.

5.6. Magnetic resonance imaging

Worth mentioning, magnetic resonance imaging (MRI) is a technology closely related to NMR that has also been used in battery science to visualize the growth patterns of dendrites [233, 234]. This magnetic resonance technique has provided insight on the unique structures present on electrodes, including dendritic formation mechanisms, the impact of cycling, and important concepts in improving the design of battery materials [234, 235]. A number of atoms that are commonly found in the cathodes, anodes, and electrolytes of batteries, such as Li, O, C, H, N, Na, Mg, etc, are suitable for detection with MRI, making it a highly relevant tool for discovery of the transformations taking place during the charge/discharge cycles of a variety of electrochemical cells. One such example is the concentration gradient of ions in electrolyte that form when current is applied. *In situ* ^{7}Li imaging was applied to demonstrate this in Li–ion systems, showing directly local differences during *in situ* operation [236]. Combining this with diffusion measurements has also provided a time and specially resolved picture of the diffusive behavior of electrolytes in a battery [237]. MRI has also been applied to show changes in the magnetic field around a battery, circumventing the need for RF penetration into the cell. In this way, changes in susceptibility related to lithiation can be observed and the potential for MRI to detect defects in a cell has been suggested, offering a powerful, non-invasive tool for battery assessment [203]. Already it has been demonstrated to aid in the understanding of the irreversible nature of degraded battery performance resulting from Li microstructures and non-uniform lithium distribution on graphite. Given the ability to visualize distributions of species (electrolytes, charges, etc) MRI provides a unique spacial description of battery cells during operation. Doubtless, with the advantages magnetic resonance imaging can provide, it will continue to be an essential asset to *in situ* battery research.

6. Concluding remarks and outlook

Given the importance of batteries in modern society, a deep understanding of these chemical systems at the molecular level is of paramount importance for continued technological advancement. Understanding the failure mechanisms and properties of different batteries will direct future research efforts to solving the key challenges in capacity, longevity, and efficiency. Herein, we have outlined the technological advances and techniques that make such discoveries possible. *In situ* NMR is truly a powerful tool for battery research and has been used as such for about two decades to better understand these electrochemical systems. We have shown the unique advantages NMR processes over other techniques and the importance of *in situ* measurement where some species can only be observed when current is applied to the real, functioning battery. Additionally, we have shown the unique advantages of conducing ^{6}Li, ^{17}O, and ^{25}Mg NMR at the ultra-high field of 850 MHz for obtaining the detailed chemical compositions in the cycled electrodes and the solvation structures of ions in electrolytes by coupling with molecular dynamics studies and DFT NMR calculations. Continued progress will be made in the area where further research will be focused on applying the newest cell designs with O-ring sealing for handling elevated temperature and pressure and 3D printed bodies for long-run studies of battery cycling. Future efforts to enhance the signal for detection of less abundant nuclei in these batteries is also an area of interest and may be realized by applying additional cells in parallel. Other

sensitivity enhancement techniques, notably, the technique of dynamic nuclear polarization (DNP) that can potentially increase an NMR signal by up to 2–4 orders of magnitude via transferring paramagnetic electron polarization from a polarization agent by taking advantage of the much larger electron Zeeman interaction [238–240], may further help to advance the application of NMR in energy storage research. One final area that lacks extensive literature is the detailed time scale information on various processes that NMR can probe [232]. Such information will provide unprecedented insight into the interaction mechanisms and molecular motion at play within these systems. Regardless of the focus of these next developments, NMR will clearly maintain importance in understanding the electrochemical process as new battery systems are developed that progressively improve our current technology as the iterative approach dictates.

Acknowledgments

This work was supported by the Joint Center for Energy Storage Research (JCESR FWP # 63076), an Energy Innovation Hub funded by the U.S. Department of Energy, Office of Science, Office of Basic Energy Sciences (BES). Pacific Northwest National Laboratory is operated by Battelle for the U.S. Department of Energy under Contract DE-AC05-76RL01830. The authors are very grateful to Ms Pamela M Warren for her help with the polishing of grammar and usage throughout the text.

ORCID iDs

Jian Zhi Hu https://orcid.org/0000-0001-8879-747X
Nicholas R Jaegers https://orcid.org/0000-0002-9930-7672
Karl Todd Mueller https://orcid.org/0000-0001-9609-9516

References

[1] Lv D P *et al* 2015 Failure mechanism for fast-charged lithium metal batteries with liquid electrolytes *Adv. Energy Mater.* **5** 1400993
[2] Winter M and Brodd R J 2004 What are batteries, fuel cells, and supercapacitors? *Chem. Rev.* **104** 4245–69
[3] Guo J, Xu Y and Wang C 2011 Sulfur-impregnated disordered carbon nanotubes cathode for lithium–sulfur batteries *Nano Lett.* **11** 4288–94
[4] Wei Seh Z *et al* 2013 Sulphur–TiO_2 yolk–shell nanoarchitecture with internal void space for long-cycle lithium–sulphur batteries *Nat. Commun.* **4** 1331
[5] Cao Y *et al* 2011 Sandwich-type functionalized graphene sheet-sulfur nanocomposite for rechargeable lithium batteries *Phys. Chem. Chem. Phys.* **13** 7660–5
[6] Suo L *et al* 2017 How solid-electrolyte interphase forms in aqueous electrolytes *J. Am. Chem. Soc.* **139** 18670–80
[7] Kissinger P T and Heineman W R 1983 Cyclic voltammetry *J. Chem. Educ.* **60** 702
[8] Nicholson R S 1965 Theory and application of cyclic voltammetry for measurement of electrode reaction kinetics *Anal. Chem.* **37** 1351–5
[9] Wang C-M 2015 *In situ* transmission electron microscopy and spectroscopy studies of rechargeable batteries under dynamic operating conditions: a retrospective and perspective view *J. Mater. Res.* **30** 326–39
[10] Wang C-M, Liao H-G and Ross F M 2015 Observation of materials processes in liquids by electron microscopy *MRS Bull.* **40** 46–52
[11] Haider M, Uhlemann S, Schwan E, Rose H, Kabius B and Urban K 1998 Electron microscopy image enhanced *Nature* **392** 768
[12] Krivanek O L, Nellist P D, Dellby N, Murfitt M F and Szilagyi Z 2003 Towards sub-0.5 Å electron beams *Ultramicroscopy* **96** 229–37
[13] Müller H, Uhlemann S, Hartel P and Haider M 2006 Advancing the hexapole Cs-corrector for the scanning transmission electron microscope *Microsc. Microanal.* **12** 442–55
[14] Batson P E, Dellby N and Krivanek O L 2002 Sub-ångstrom resolution using aberration corrected electron optics *Nature* **418** 617
[15] Kisielowski C *et al* 2008 Detection of single atoms and buried defects in three dimensions by aberration-corrected electron microscope with 0.5 Å information limit *Microsc. Microanal.* **14** 469–77
[16] Muller D A 2009 Structure and bonding at the atomic scale by scanning transmission electron microscopy *Nat. Mater.* **8** 263
[17] Retoux R, Brousse T and Schleich D M 1999 High-resolution electron microscopy investigation of capacity fade in SnO_2 electrodes for lithium-ion batteries *J. Electrochem. Soc.* **146** 2472–6
[18] Laffont L *et al* 2006 Study of the $LiFePO_4/FePO_4$ two-phase system by high-resolution electron energy loss spectroscopy *Chem. Mater.* **18** 5520–9
[19] McDowell M T and Cui Y 2011 Single nanostructure electrochemical devices for studying electronic properties and structural changes in lithiated Si nanowires *Adv. Energy Mater.* **1** 894–900
[20] Wang C M *et al* 2010 *In situ* transmission electron microscopy and spectroscopy studies of interfaces in Li ion batteries: challenges and opportunities *J.Mater. Res.* **25** 1541–7
[21] Huang J Y *et al* 2010 *In Situ* observation of the electrochemical lithiation of a single SnO_2 nanowire electrode *Science* **330** 1515
[22] Liu X H, Zhong L, Huang S, Mao S X, Zhu T and Huang J Y 2012 Size-dependent fracture of silicon nanoparticles during lithiation *ACS Nano* **6** 1522–31
[23] Liu X H, Huang S, Picraux S T, Li J, Zhu T and Huang J Y 2011 Reversible nanopore formation in Ge nanowires during lithiation–delithiation cycling: an *in situ* transmission electron microscopy study *Nano Lett.* **11** 3991–7
[24] Liu Y, Hudak N S, Huber D L, Limmer S J, Sullivan J P and Huang J Y 2011 *In situ* transmission electron microscopy observation of pulverization of aluminum nanowires and evolution of the thin surface Al_2O_3 layers during lithiation–delithiation cycles *Nano Lett.* **11** 4188–94
[25] Zhang L Q *et al* 2012 Direct observation of Sn crystal growth during the lithiation and delithiation processes of SnO_2 nanowires *Micron* **43** 1127–33
[26] Kushima A, Liu X H, Zhu G, Wang Z L, Huang J Y and Li J 2011 Leapfrog cracking and nanoamorphization of ZnO nanowires during *in situ* electrochemical lithiation *Nano Lett.* **11** 4535–41
[27] Liu X H *et al* 2012 *In situ* transmission electron microscopy of electrochemical lithiation, delithiation and deformation of individual graphene nanoribbons *Carbon* **50** 3836–44
[28] Li Q *et al* 2014 *In situ* TEM on the reversibility of nanosized sn anodes during the electrochemical reaction *Chem. Mater.* **26** 4102–8
[29] Wang F *et al* 2012 Tracking lithium transport and electrochemical reactions in nanoparticles *Nat. Commun.* **3** 1201

[30] Liu X H *et al* 2011 Anisotropic swelling and fracture of silicon nanowires during lithiation *Nano Lett.* **11** 3312–8

[31] Liu X H *et al* 2011 Ultrafast electrochemical lithiation of individual Si nanowire anodes *Nano Lett.* **11** 2251–8

[32] Williamson M J, Tromp R M, Vereecken P M, Hull R and Ross F M 2003 Dynamic microscopy of nanoscale cluster growth at the solid–liquid interface *Nat. Mater.* **2** 532

[33] Woehl T J, Park C, Evans J E, Arslan I, Ristenpart W D and Browning N D 2014 Direct observation of aggregative nanoparticle growth: kinetic modeling of the size distribution and growth rate *Nano Lett.* **14** 373–8

[34] Gu M *et al* 2013 Demonstration of an electrochemical liquid cell for operando transmission electron microscopy observation of the lithiation/delithiation behavior of Si nanowire battery anodes *Nano Lett.* **13** 6106–12

[35] Holtz M E *et al* 2014 Nanoscale imaging of lithium ion distribution during *in situ* operation of battery electrode and electrolyte *Nano Lett.* **14** 1453–9

[36] Sacci R L *et al* 2014 Direct visualization of initial SEI morphology and growth kinetics during lithium deposition by *in situ* electrochemical transmission electron microscopy *Chem. Commun.* **50** 2104–7

[37] Unocic R R *et al* 2014 Quantitative electrochemical measurements using *in situ* ec-S/TEM devices *Microsc. Microanal.* **20** 452–61

[38] Kong F *et al* 2001 *In situ* studies of SEI formation *J. Power Sources* **97–8** 58–66

[39] Inaba M, Iriyama Y, Ogumi Z, Todzuka Y and Tasaka A 1997 Raman study of layered rock-salt $LiCoO_2$ and its electrochemical lithium deintercalation *J. Raman Spectrosc.* **28** 613–7

[40] Hardwick L J *et al* 2006 An *in situ* Raman study of the intercalation of supercapacitor-type electrolyte into microcrystalline graphite *Electrochim. Acta* **52** 675–80

[41] Hardwick L J, Ruch P W, Hahn M, Scheifele W, Kötz R and Novák P 2008 *In situ* Raman spectroscopy of insertion electrodes for lithium-ion batteries and supercapacitors: first cycle effects *J. Phys. Chem. Solids* **69** 1232–7

[42] Dokko K, Mohamedi M, Anzue N, Itoh T and Uchida I 2002 *In situ* Raman spectroscopic studies of $LiNi_xMn_{2-x}O_4$ thin film cathode materials for lithium ion secondary batteries *J. Mater. Chem.* **12** 3688–93

[43] Wu H-L, Huff L A and Gewirth A A 2015 *In situ* Raman spectroscopy of sulfur speciation in lithium–sulfur batteries *ACS Appl. Mater. Interfaces* **7** 1709–19

[44] Park Y *et al* 2017 Reaction at the electrolyte–electrode interface in a Li–ion battery studied by *in situ* Raman spectroscopy *Bull. Korean Chem. Soc.* **38** 511–3

[45] Nanda J, Datta M K, Remillard J T, O'Neill A and Kumta P N 2009 *In situ* Raman microscopy during discharge of a high capacity silicon–carbon composite Li–ion battery negative electrode *Electrochem. Commun.* **11** 235–7

[46] Zhang X and Frech R 1998 *In situ* Raman spectroscopy of $Li_xV_2O_5$ in a lithium rechargeable battery *J. Electrochem. Soc.* **145** 847–51

[47] Yamanaka T *et al* 2017 *In situ* Raman spectroscopic studies on concentration change of ions in the electrolyte solution in separator regions in a lithium ion battery by using multi-microprobes *Electrochem. Commun.* **77** 32–5

[48] Yamanaka T *et al* 2017 *In situ* Raman spectroscopic studies on concentration change of electrolyte salt in a lithium ion model battery with closely faced graphite composite and $LiCoO_2$ composite electrodes by using an ultrafine microprobe *Electrochim. Acta* **234** 93–8

[49] Patel Manu U M, Demir-Cakan R, Morcrette M, Tarascon J M, Gaberscek M and Dominko R 2013 Li–S battery analyzed by UV/Vis in operando mode *ChemSusChem* **6** 1177–81

[50] Aurbach D and Chusid O 1997 The use of *in situ* Fourier-transform infrared spectroscopy for the study of surface phenomena on electrodes in selected lithium battery electrolyte solutions *J. Power Sources* **68** 463–70

[51] Song S-W and Baek S-W 2009 Silane-derived SEI stabilization on thin-film electrodes of nanocrystalline Si for lithium batteries *Electrochem. Solid-State Lett.* **12** A23–27

[52] Sun F *et al* 2018 Correlating morphological evolution of Li electrodes with degrading electrochemical performance of Li/$LiCoO_2$ and Li/S battery systems: investigated by synchrotron x-ray phase contrast tomography *ACS Energy Lett.* **3** 356–65

[53] Nelson J *et al* 2012 In operando x-ray diffraction and transmission x-ray microscopy of lithium sulfur batteries *J. Am. Chem. Soc.* **134** 6337–43

[54] Dahn J R 1991 Phase diagram of Li_xC_6 *Phys. Rev.* B **44** 9170–7

[55] Walus S *et al* 2013 New insight into the working mechanism of lithium–sulfur batteries: *in situ* and operando x-ray diffraction characterization *Chem. Commun.* **49** 7899–901

[56] Hatchard T D and Dahn J R 2004 *In situ* XRD and electrochemical study of the reaction of lithium with amorphous silicon *J. Electrochem. Soc.* **151** A838–42

[57] Poizot P, Laruelle S, Grugeon S, Dupont L and Tarascon J M 2000 Nano-sized transition-metal oxides as negative-electrode materials for lithium-ion batteries *Nature* **407** 496

[58] Yao K P C, Kwabi D G, Quinlan R A, Mansour A N, Grimaud A, Lee Y-L, Lu Y-C and Shao-Horn Y 2013 Thermal stability of Li_2O_2 and Li_2O for Li–air batteries: *in situ* XRD and XPS studies *J. Electrochem. Soc.* **160** A824–31

[59] Chan C K *et al* 2007 High-performance lithium battery anodes using silicon nanowires *Nat. Nanotechnol.* **3** 31

[60] Balasubramanian M, Sun X, Yang X Q and McBreen J 2001 *In situ* x-ray diffraction and x-ray absorption studies of high-rate lithium-ion batteries *J. Power Sources* **92** 1–8

[61] Yoon W-S, Chung K Y, McBreen J and Yang X-Q 2006 A comparative study on structural changes of $LiCo_{1/3}Ni_{1/3}Mn_{1/3}O_2$ and $LiNi_{0.8}Co_{0.15}Al_{0.05}O_2$ during first charge using *in situ* XRD *Electrochem. Commun.* **8** 1257–62

[62] Guo J-Z *et al* 2017 High-energy/power and low-temperature cathode for sodium-ion batteries: *in situ* XRD study and superior full-cell performance *Adv. Mater.* **29** 1701968

[63] Ou X *et al* 2017 *In situ* X-ray diffraction characterization of $NiSe_2$ as a promising anode material for sodium ion batteries *J. Power Sources* **343** 483–91

[64] Cuisinier M *et al* 2013 Sulfur speciation in Li–S batteries determined by operando x-ray absorption spectroscopy *J. Phys. Chem. Lett.* **4** 3227–32

[65] Gao J, Lowe M A, Kiya Y and Abruña H D 2011 Effects of liquid electrolytes on the charge–discharge performance of rechargeable lithium/sulfur batteries: electrochemical and *in situ* x-ray absorption spectroscopic studies *J. Phys. Chem.* C **115** 25132–7

[66] Tang C Y, Haasch R T and Dillon S J 2016 *In situ* x-ray photoelectron and Auger electron spectroscopic characterization of reaction mechanisms during Li–ion cycling *Chem. Commun.* **52** 13257–60

[67] Bryngelsson H, Stjerndahl M, Gustafsson T and Edström K 2017 How dynamic is the SEI? *J. Power Sources* **174** 970–5

[68] Lu Y C *et al* 2012 *In situ* ambient pressure x-ray photoelectron spectroscopy studies of lithium-oxygen redox reactions *Sci. Rep.* **2** 715

[69] Nandasiri M I *et al* 2017 *In Situ* chemical imaging of solid-electrolyte interphase layer evolution in Li–S batteries *Chem. Mater.* **29** 4728–37

[70] Kondekar N P, Boebinger M G, Woods E V and McDowell M T 2017 *In Situ* XPS investigation of

transformations at crystallographically oriented MoS_2 interfaces *ACS Appl. Mater. Interfaces* **9** 32394–404
[71] Lahiri A, Borisenko N, Olschewski M, Pulletikurthi G and Endres F 2018 Anomalous electroless deposition of less noble metals on Cu in ionic liquids and its application towards battery electrodes *Faraday Discuss.* **206** 339–51
[72] Andersson A M, Abraham D P, Haasch R, MacLaren S, Liu J and Amine K 2002 Surface characterization of electrodes from high power lithium-ion batteries *J. Electrochem. Soc.* **149** A1358–69
[73] Bhattacharyya R, Key B, Chen H, Best A S, Hollenkamp A F and Grey C P 2010 *In situ* NMR observation of the formation of metallic lithium microstructures in lithium batteries *Nat. Mater.* **9** 504
[74] Deng X *et al* 2015 Natural abundance ^{17}O nuclear magnetic resonance and computational modeling studies of lithium based liquid electrolytes *J. Power Sources* **285** 146–55
[75] Zhao Z C *et al* 2017 Mechanism of phenol alkylation in zeolite H-BEA using *in situ* solid-state NMR spectroscopy *J. Am. Chem. Soc.* **139** 9178–85
[76] Zhao Z C, Xu S C, Hu M Y, Bao X H and Hu J Z 2016 *In situ* high temperature high pressure MAS NMR study on the crystallization of AlPO4-5 *J. Phys. Chem.* C **120** 1701–8
[77] Jaegers N R, Hu M Y, Hoyt D W, Wang Y and Hu J Z 2017 Development and application of *in situ* high-temperature, high-pressure magic angle spinning NMR *Modern Magnetic Resonance* ed G A Webb (Cham: Springer) pp 1–19
[78] Abbrent S and Greenbaum S 2013 Recent progress in NMR spectroscopy of polymer electrolytes for lithium batteries *Curr. Opin. Colloid Interface Sci.* **18** 228–44
[79] Trease N M, Köster T K J and Grey C P 2011 *In situ* NMR studies of lithium ion batteries *Electrochem. Soc. Interface* **20** 69–73
[80] Blanc F, Leskes M and Grey C P 2013 *In situ* solid-state NMR spectroscopy of electrochemical cells: batteries, supercapacitors, and fuel cells *Acc. Chem. Res.* **46** 1952–63
[81] Harks P P R M L, Mulder F M and Notten P H L 2015 *In situ* methods for Li–ion battery research: a review of recent developments *J. Power Sources* **288** 92–105
[82] Wishart D S and Case D A 2001 Use of chemical shifts in macromolecular structure determination *Nucl. Magn. Reson. Biol. Macromol.* A **338** 3–34
[83] Hu J Z *et al* 2018 Mg-25 NMR and computational modeling studies of the solvation structures and molecular dynamics in magnesium based liquid electrolytes *Nano Energy* **46** 436–46
[84] Clore G M and Iwahara J 2009 Theory, practice, and applications of paramagnetic relaxation enhancement for the characterization of transient low-population states of biological macromolecules and their complexes *Chem. Rev.* **109** 4108–39
[85] Bryant R G 1983 The nmr time scale *J. Chem. Educ.* **60** 933–5
[86] Jeener J, Meier B H, Bachmann P and Ernst R R 1979 Investigation of exchange processes by 2-dimensional Nmr-spectroscopy *J. Chem. Phys.* **71** 4546–53
[87] Palmer A G, Grey M J and Wang C Y 2005 Solution NMR spin relaxation methods for characterizing chemical exchange in high-molecular-weight systems *Nucl. Magn. Reson. Biol. Macromol.* C **394** 430–65
[88] Kleckner I R and Foster M P 2011 An introduction to NMR-based approaches for measuring protein dynamics *Biochim. Biophys. Acta Proteins Proteom.* **1814** 942–68
[89] Lipari G and Szabo A 1982 Model-free approach to the interpretation of nuclear magnetic-resonance relaxation in macromolecules. 2. analysis of experimental results *J. Am. Chem. Soc.* **104** 4559–70
[90] Bloembergen N, Purcell E M and Pound R V 1948 Relaxation effects in nuclear magnetic resonance absorption *Phys. Rev.* **73** 679–712
[91] Hallenga K and Koenig S H 1976 Protein rotational relaxation as studied by solvent proton and deuteron magnetic relaxation *Biochemistry* **15** 4255–64
[92] Massi F, Johnson E, Wang C Y, Rance M and Palmer A G 2004 NMR R-1 rho rotating-frame relaxation with weak radio frequency fields *J. Am. Chem. Soc.* **126** 2247–56
[93] Deverell C, Morgan R E and Strange J H 1970 Studies of chemical exchange by nuclear magnetic relaxation in rotating frame *Mol. Phys.* **18** 553
[94] Korzhnev D M, Skrynnikov N R, Millet O, Torchia D A and Kay L E 2002 An NMR experiment for the accurate measurement of heteronuclear spin-lock relaxation rates *J. Am. Chem. Soc.* **124** 10743–53
[95] Pecher O, Carretero-Gonzalez J, Griffith K J and Grey C P 2017 Materials' methods: NMR in battery research *Chem. Mater.* **29** 213–42
[96] Xiao J *et al* 2015 Following the transient reactions in lithium-sulfur batteries using an *in situ* nuclear magnetic resonance technique *Nano Lett.* **15** 3309–16
[97] Tang W *et al* 2015 Probing lithium germanide phase evolution and structural change in a germanium-in-carbon nanotube energy storage system *J. Am. Chem. Soc.* **137** 2600–7
[98] Rathke J W, Klingler R J, Gerald R E, Kramarz K W and Woelk K 1997 Toroids in NMR spectroscopy *Progr. Nucl. Magn. Reson. Spectrosc.* **30** 209–53
[99] Rathke J W 1989 Toroid detectors in pressure probes *J. Magn. Reson.* **85** 150–5
[100] Rathke J W, Klingler R J, Woelk K and Rex E G I 2000 Near-electrode imager *US Patent No.* 6,046,592
[101] Gerald R E, Johnson C S, Rathke J W, Klingler R J, Sandí G and Scanlon L G 2000 ^{7}Li NMR study of intercalated lithium in curved carbon lattices *J. Power Sources* **89** 237–43
[102] Gerald I R E, Sanchez J, Johnson C S, Klingler R J and Rathke J W 2001 *In situ* nuclear magnetic resonance investigations of lithium ions in carbon electrode materials using a novel detector *J. Phys.: Condens. Matter* **13** 8269
[103] Tarascon J M, Gozdz A S, Schmutz C, Shokoohi F and Warren P C 1996 Performance of Bellcore's plastic rechargeable Li–ion batteries *Solid State Ion.* **86–8** 49–54
[104] Chevallier F *et al* 2003 *In situ* ^{7}Li-nuclear magnetic resonance observation of reversible lithium insertion into disordered carbons *Electrochem. Solid-State Lett.* **6** A225–8
[105] Letellier M *et al* 2003 The first *in situ* ^{7}Li nuclear magnetic resonance study of lithium insertion in hard-carbon anode materials for Li–ion batteries *J. Chem. Phys.* **118** 6038–45
[106] Pecher O, Bayley P M, Liu H, Liu Z G, Trease N M and Grey C P 2016 Automatic tuning matching cycler (ATMC) *in situ* NMR spectroscopy as a novel approach for real-time investigations of Li- and Na–ion batteries *J. Magn. Reson.* **265** 200–9
[107] Letellier M, Chevallier F and Morcrette M 2007 *In situ* ^{7}Li nuclear magnetic resonance observation of the electrochemical intercalation of lithium in graphite; 1st cycle *Carbon* **45** 1025–34
[108] Zaghib K, Tatsumi K, Sawada Y, Higuchi S, Abe H and Ohsaki T 1999 ^{7}Li-NMR of well-graphitized vapor-grown carbon fibers and natural graphite negative electrodes of rechargeable lithium-ion batteries *J. Electrochem. Soc.* **146** 2784–93
[109] Tatsumi K *et al* 1996 ^{7}Li-nuclear magnetic resonance observation of lithium insertion into mesocarbon microbeads *J. Electrochem. Soc.* **143** 1923–30
[110] Tatsumi K *et al* 1999 Low temperature ^{7}Li-NMR investigations on lithium inserted into carbon anodes for rechargeable lithium-ion cells *J. Power Sources* **81–2** 397–400

[111] Poli F, Kshetrimayum J S, Monconduit L and Letellier M 2011 New cell design for *in situ* NMR studies of lithium-ion batteries *Electrochem. Commun.* **13** 1293–5

[112] Chen H *et al* 2014 Micro-battery development for juvenile salmon acoustic telemetry system applications *Sci. Rep.* **4** 3790

[113] Tang W *et al* 2016 *In situ* Raman and nuclear magnetic resonance study of trapped lithium in the solid electrolyte interface of reduced graphene oxide *J. Phys. Chem.* C **120** 2600–8

[114] Hu J Z *et al* 2016 *In situ* ^{7}Li and ^{133}Cs nuclear magnetic resonance investigations on the role of Cs+ additive in lithium-metal deposition process *J. Power Sources* **304** 51–9

[115] Key B, Bhattacharyya R, Morcrette M, Seznéc V, Tarascon J-M and Grey C P 2009 Real-time NMR investigations of structural changes in silicon electrodes for lithium-ion batteries *J. Am. Chem. Soc.* **131** 9239–49

[116] Kayser S A, Mester A, Mertens A, Jakes P, Eichel R A and Granwehr J 2018 Long-run in operando NMR to investigate the evolution and degradation of battery cells *Phys. Chem. Chem. Phys.* **20** 13765–76

[117] Arai J, Gotoh K, Sayama R and Takeda K 2017 Slow stabilization of Si–Li alloys formed during charge and discharge of a Si–C mixed electrode studied by *in situ* solid-state ^{7}Li nuclear magnetic resonance spectroscopy *J. Electrochem. Soc.* **164** A6334–40

[118] Trease N M, Zhou L, Chang H J, Zhu B Y and Grey C P 2012 *In situ* NMR of lithium ion batteries: bulk susceptibility effects and practical considerations *Solid State Nucl. Magn. Reson.* **42** 62–70

[119] Wiemers-Meyer S, Winter M and Nowak S 2017 A battery cell for *in situ* NMR measurements of liquid electrolytes *Phys. Chem. Chem. Phys.* **19** 4962–6

[120] Huo H, Chamas M, Lippens P-E and Ménétrier M 2012 Multinuclear NMR study of the solid electrolyte interface on the Li–$FeSn_2$ negative electrodes for Li–ion batteries *J. Phys. Chem.* C **116** 2390–8

[121] Paik Y, Osegovic J P, Wang F, Bowden W and Grey C P 2001 2H MAS NMR studies of the manganese dioxide tunnel structures and hydroxides used as cathode materials in primary batteries *J. Am. Chem. Soc.* **123** 9367–77

[122] Allcock H R, Napierala M E, Olmeijer D L, Best S A and Merz K M 1999 Ionic conduction in polyphosphazene solids and gels: ^{13}C, ^{31}P, and ^{15}N NMR spectroscopy and molecular dynamics simulations *Macromolecules* **32** 732–41

[123] Bogle X, Vazquez R, Greenbaum S, von Cresce A W and Xu K 2013 Understanding Li+–solvent interaction in nonaqueous carbonate electrolytes with ^{17}O NMR *J. Phys. Chem. Lett.* **4** 1664–8

[124] Lee J, Seymour I D, Pell A J, Dutton S E and Grey C P 2017 A systematic study of ^{25}Mg NMR in paramagnetic transition metal oxides: applications to Mg-ion battery materials *Phys. Chem. Chem. Phys.* **19** 613–25

[125] Guo B *et al* 2008 Electrochemical reduction of nano-SiO_2 in hard carbon as anode material for lithium ion batteries *Electrochem. Commun.* **10** 1876–8

[126] Vijayakumar M *et al* 2011 Towards understanding the poor thermal stability of V5+ electrolyte solution in vanadium redox flow batteries *J. Power Sources* **196** 3669–72

[127] Andrew E R, Bradbury A and Eades R G 1958 Nuclear magnetic resonance spectra from a crystal rotated at high speed *Nature* **182** 1659

[128] Dupre N, Martin J-F, Guyomard D, Yamada A and Kanno R 2008 Detection of surface layers using ^{7}Li MAS NMR *J. Mater. Chem.* **18** 4266–73

[129] Marino C *et al* 2013 Study of the electrode/electrolyte interface on cycling of a conversion type electrode material in Li batteries *J. Phys. Chem.* C **117** 19302–13

[130] Hu Y-Y *et al* 2013 Origin of additional capacities in metal oxide lithium-ion battery electrodes *Nat. Mater.* **12** 1130

[131] Key B, Morcrette M, Tarascon J M and Grey C P 2011 Pair distribution function analysis and solid state NMR studies of silicon electrodes for lithium ion batteries: understanding the (De)lithiation mechanisms *J. Am. Chem. Soc.* **133** 503–12

[132] Grey C P and Dupré N 2004 NMR studies of cathode materials for lithium-ion rechargeable batteries *Chem. Rev.* **104** 4493–512

[133] Rao K S, Sridhar R and Susila S 1981 The charge form factor and the quadrupole moment of ^{7}Li *Phys. Scr* **24** 925

[134] Cheon I-T 1969 Charge form factor and quadrupole moment of ^{6}Li *Phys. Lett.* B **30** 81–4

[135] Kerisit S, Vijayakumar M, Han K S and Mueller K T 2015 Solvation structure and transport properties of alkali cations in dimethyl sulfoxide under exogenous static electric fields *J. Chem. Phys.* **142** 224502

[136] Han K S *et al* 2016 Preferential solvation of an asymmetric redox molecule *J. Phys. Chem.* C **120** 27834–9

[137] Wei X *et al* 2014 Towards high-performance nonaqueous redox flow electrolyte via ionic modification of active species *Adv. Energy Mater.* **5** 1400678

[138] Huang J *et al* 2018 A two-electron storage nonaqueous organic redox flow Battery *Adv. Sustain. Syst.* **2** 1700131

[139] Vijayakumar M *et al* 2014 Understanding aqueous electrolyte stability through combined computational and magnetic resonance spectroscopy: a case study on vanadium redox flow battery electrolytes *ChemPlusChem* **80** 428–37

[140] Vijayakumar M, Wang W, Nie Z, Sprenkle V and Hu J 2013 Elucidating the higher stability of vanadium(V) cations in mixed acid based redox flow battery electrolytes *J. Power Sources* **241** 173–7

[141] Li L *et al* 2011 A Stable vanadium redox-flow battery with high energy density for large-scale energy storage *Adv. Energy Mater.* **1** 394–400

[142] Kim S *et al* 2011 Chloride supporting electrolytes for all-vanadium redox flow batteries *Phys. Chem. Chem. Phys.* **13** 18186–93

[143] Cosimbescu L *et al* 2015 Anion-tunable properties and electrochemical performance of functionalized ferrocene compounds *Sci. Rep.* **5** 14117

[144] Li B *et al* 2015 Ambipolar zinc-polyiodide electrolyte for a high-energy density aqueous redox flow battery *Nat. Commun.* **6** 6303

[145] Wang W, Luo Q, Li B, Wei X, Li L and Yang Z 2012 Recent progress in redox flow battery research and development *Adv. Funct. Mater.* **23** 970–86

[146] Mai Z, Zhang H, Li X, Bi C and Dai H 2011 Sulfonated poly(tetramethydiphenyl ether ether ketone) membranes for vanadium redox flow battery application *J. Power Sources* **196** 482–7

[147] Parasuraman A, Lim T M, Menictas C and Skyllas-Kazacos M 2013 Review of material research and development for vanadium redox flow battery applications *Electrochim. Acta* **101** 27–40

[148] Mohammadi T and Skyllas-Kazacos M 1995 Characterisation of novel composite membrane for redox flow battery applications *J. Membr. Sci.* **98** 77–87

[149] Bamine T *et al* 2017 Understanding local defects in Li–ion battery electrodes through combined DFT/NMR studies: application to LiVPO4F *J. Phys. Chem.* C **121** 3219–27

[150] Gregor T, Mauri F and Car R 1999 A comparison of methods for the calculation of NMR chemical shifts *J. Chem. Phys.* **111** 1815–22

[151] Schreckenbach G and Ziegler T 1995 Calculation of NMR shielding tensors using gauge-including atomic orbitals and modern density functional theory *J. Phys. Chem.* **99** 606–11

[152] Wolinski K, Hinton J F and Pulay P 1990 Efficient implementation of the gauge-independent atomic orbital method for NMR chemical shift calculations *J. Am. Chem. Soc.* **112** 8251–60

[153] Rauhut G, Puyear S, Wolinski K and Pulay P 1996 Comparison of NMR shieldings calculated from Hartree–Fock and density functional wave functions using gauge-including atomic orbitals *J. Phys. Chem.* **100** 6310–6

[154] Pickard C J and Mauri F 2001 All-electron magnetic response with pseudopotentials: NMR chemical shifts *Phys. Rev.* B **63** 245101–13

[155] Segall M D *et al* 2002 First-principles simulation: ideas, illustrations and the CASTEP code *J. Phys.: Condens. Matter* **14** 2717–44

[156] Schreckenbach G and Ziegler T 1998 The calculation of NMR shielding tensors based on density functional theory and the frozen-core approximation *Int. J. Quantum Chem.* **60** 753–66

[157] Seymour I D, Middlemiss D S, Halat D M, Trease N M, Pell A J and Grey C P 2016 Characterizing oxygen local environments in paramagnetic battery materials via ^{17}O NMR and DFT calculations *J. Am. Chem. Soc.* **138** 9405–8

[158] Klamt A and Schuurmann G 1993 COSMO: a new approach to dielectric screening in solvents with explicit expressions for the screening energy and its gradient *J. Chem. Soc., Perkin Trans.* **2** 799–805

[159] Korth M 2014 Large-scale virtual high-throughput screening for the identification of new battery electrolyte solvents: evaluation of electronic structure theory methods *Phys. Chem. Chem. Phys.* **16** 7919–26

[160] Muldoon J *et al* 2012 Electrolyte roadblocks to a magnesium rechargeable battery *Energy Environ. Sci.* **5** 5941–50

[161] Schreckenbach G and Ziegler T 1998 Calculation of NMR shielding tensors based on density functional theory and a scalar relativistic Pauli-type hamiltonian. The application to transition metal complexes *Int. J. Quantum Chem.* **61** 899–918

[162] Wolff S K, Ziegler T, van Lenthe E and Baerends E J 1999 Density functional calculations of nuclear magnetic shieldings using the zeroth-order regular approximation (ZORA) for relativistic effects: ZORA nuclear magnetic resonance *J. Chem. Phys.* **110** 7689–98

[163] van Lenthe E, Baerends E J and Snijders J G 1993 Relativistic regular two-component Hamiltonians *J. Chem. Phys.* **99** 4597–610

[164] Sadhukhan M and Tkatchenko A 2017 Long-range repulsion between spatially confined van der waals dimers *Phys. Rev. Lett.* **118** 210402

[165] Kühne Thomas D 2014 Second generation car–parrinello molecular dynamics *Wiley Interdiscip. Rev.: Comput. Mol. Sci.* **4** 391–406

[166] Tasaki K, Kanda K, Nakamura S and Ue M 2003 Decomposition of $LiPF_6$ and stability of PF_5 in Li–ion battery electrolytes: density functional theory and molecular dynamics studies *J. Electrochem. Soc.* **150** A1628–36

[167] Tasaki K 2005 Solvent decompositions and physical properties of decomposition compounds in Li–ion battery electrolytes studied by DFT calculations and molecular dynamics simulations *J. Phys. Chem.* B **109** 2920–33

[168] Leung K and Budzien J L 2010 *Ab initio* molecular dynamics simulations of the initial stages of solid-electrolyte interphase formation on lithium ion battery graphitic anodes *Phys. Chem. Chem. Phys.* **12** 6583–6

[169] Ganesh P, Kent P R C and Jiang D-E 2012 Solid–electrolyte interphase formation and electrolyte reduction at Li–ion battery graphite anodes: insights from first-principles molecular dynamics *J. Phys. Chem.* C **116** 24476–81

[170] Bedrov D, Smith G D and van Duin A C T 2012 Reactions of singly-reduced ethylene carbonate in lithium battery electrolytes: a molecular dynamics simulation study using the ReaxFF *J. Phys. Chem.* A **116** 2978–85

[171] Ganesh P, Jiang D-E and Kent P R C 2011 Accurate static and dynamic properties of liquid electrolytes for Li–ion batteries from *ab initio* molecular dynamics *J. Phys. Chem.* B **115** 3085–90

[172] Truflandier L A and Autschbach J 2010 Probing the solvent shell with ^{195}Pt chemical shifts: density functional theory molecular dynamics study of PtII and PtIV anionic complexes in aqueous solution *J. Am. Chem. Soc.* **132** 3472–83

[173] Sterzel M and Autschbach J 2006 Toward an accurate determination of ^{195}Pt chemical shifts by density functional computations: the importance of unspecific solvent effects and the dependence of Pt magnetic shielding constants on structural parameters *Inorg. Chem.* **45** 3316–24

[174] Truflandier L A, Sutter K and Autschbach J 2011 Solvent effects and dynamic averaging of ^{195}Pt NMR shielding in cisplatin derivatives *Inorg. Chem.* **50** 1723–32

[175] Idota Y, Kubota T, Matsufuji A, Maekawa Y and Miyasaka T 1997 Tin-based amorphous oxide: a high-capacity lithium-ion-storage material *Science* **276** 1395–7

[176] Xu Y *et al* 2013 Uniform nano-Sn/C composite anodes for lithium ion batteries *Nano Lett.* **13** 470–4

[177] Kennedy T, Mullane E, Geaney H, Osiak M, O'Dwyer C and Ryan K M 2014 High-performance germanium nanowire-based lithium-ion battery anodes extending over 1000 cycles through *in situ* formation of a continuous porous network *Nano Lett.* **14** 716–23

[178] Magasinski A, Dixon P, Hertzberg B, Kvit A, Ayala J and Yushin G 2010 High-performance lithium-ion anodes using a hierarchical bottom-up approach *Nat. Mater.* **9** 353

[179] Kim H, Son Y, Park C, Cho J and Choi Hee C 2013 Catalyst-free direct growth of a single to a few layers of graphene on a germanium nanowire for the anode material of a lithium battery *Angew. Chem., Int. ed* **52** 5997–6001

[180] Chan C K, Zhang X F and Cui Y 2008 High capacity Li ion battery anodes using Ge nanowires *Nano Lett.* **8** 307–9

[181] Yuan F-W, Yang H-J and Tuan H-Y 2012 Alkanethiol-passivated Ge nanowires as high-performance anode materials for lithium-ion batteries: the role of chemical surface functionalization *ACS Nano* **6** 9932–42

[182] Seo M-H, Park M, Lee K T, Kim K, Kim J and Cho J 2011 High performance Ge nanowire anode sheathed with carbon for lithium rechargeable batteries *Energy Environ. Sci.* **4** 425–8

[183] Baggetto L and Notten P H L 2009 Lithium-ion (De) insertion reaction of germanium thin-film electrodes: an electrochemical and *in situ* XRD study *J. Electrochem. Soc.* **156** A169–75

[184] Chang H J *et al* 2015 Investigating Li microstructure formation on Li anodes for lithium batteries by *in situ* ^{6}Li/^{7}Li NMR and SEM *J. Phys. Chem.* C **119** 16443–51

[185] Jung H *et al* 2015 Elucidation of the local and long-range structural changes that occur in germanium anodes in lithium-ion batteries *Chem. Mater.* **27** 1031–41

[186] Kang K, Meng Y S, Bréger J, Grey C P and Ceder G 2006 Electrodes with high power and high capacity for rechargeable lithium batteries *Science* **311** 977

[187] Wu F *et al* 2011 Sulfur/polythiophene with a core/shell structure: synthesis and electrochemical properties of the cathode for rechargeable lithium batteries *J. Phys. Chem.* C **115** 6057–63

[188] Bruce P G, Freunberger S A, Hardwick L J and Tarascon J-M 2011 Li–O_2 and Li–S batteries with high energy storage *Nat. Mater.* **11** 19

[189] Aurbach D, Pollak E, Elazari R, Salitra G, Kelley C S and Affinito J 2009 On the surface chemical aspects of very high energy density, rechargeable Li–Sulfur batteries *J. Electrochem. Soc.* **156** A694–702

[190] See K A *et al* 2014 *Ab initio* structure search and *in situ* ^{7}Li NMR studies of discharge products in the Li–S battery system *J. Am. Chem. Soc.* **136** 16368–77

[191] Kawase A, Shirai S, Yamoto Y, Arakawa R and Takata T 2014 Electrochemical reactions of lithium-sulfur batteries: an analytical study using the organic conversion technique *Phys. Chem. Chem. Phys.* **16** 9344–50

[192] Huff L A, Rapp J L, Baughman J A, Rinaldi P L and Gewirth A A 2015 Identification of lithium–sulfur battery discharge products through ^{6}Li and ^{33}S solid-state MAS and 7Li solution NMR spectroscopy *Surf. Sci.* **631** 295–300

[193] Shimoda K, Murakami M, Takamatsu D, Arai H, Uchimoto Y and Ogumi Z 2013 *In situ* NMR observation of the lithium extraction/insertion from $LiCoO_2$ cathode *Electrochim. Acta* **108** 343–9

[194] Yoshio M, Wang H, Fukuda K, Hara Y and Adachi Y 2000 Effect of carbon coating on electrochemical performance of treated natural graphite as lithium-ion battery anode material *J. Electrochem. Soc.* **147** 1245–50

[195] Hassoun J *et al* 2014 An advanced lithium-ion battery based on a graphene anode and a lithium iron phosphate cathode *Nano Lett.* **14** 4901–6

[196] Mukherjee R *et al* 2014 Defect-induced plating of lithium metal within porous graphene networks *Nat. Commun.* **5** 3710

[197] Winter M, Novák P and Monnier A 1998 Graphites for lithium-ion cells: the correlation of the first-cycle charge loss with the Brunauer–Emmett–Teller surface area *J. Electrochem. Soc.* **145** 428–36

[198] Park K H *et al* 2014 Defect-free, size-tunable graphene for high-performance lithium ion battery *Nano Lett.* **14** 4306–13

[199] Simon P and Gogotsi Y 2013 Capacitive energy storage in nanostructured carbon–electrolyte systems *Acc. Chem. Res.* **46** 1094–103

[200] Kucinskis G, Bajars G and Kleperis J 2013 Graphene in lithium ion battery cathode materials: a review *J. Power Sources* **240** 66–79

[201] Ogata K *et al* 2014 Revealing lithium–silicide phase transformations in nano-structured silicon-based lithium ion batteries via *in situ* NMR spectroscopy *Nat. Commun.* **5** 3217

[202] Hu J Z, Kwak J H, Yang Z, Osborn W, Markmaitree T and Shaw L L 2008 Investigation of mechanical activation on Li–N–H systems using ^{6}Li magic angle spinning nuclear magnetic resonance at ultra-high field *J. Power Sources* **182** 278–83

[203] Klett M *et al* 2012 Quantifying mass transport during polarization in a Li ion battery electrolyte by *in situ* ^{7}Li NMR imaging *J. Am. Chem. Soc.* **134** 14654–7

[204] Whittingham M S 2012 History, evolution, and future status of energy storage *Proc. IEEE* **100** 1518–34

[205] Aurbach D, Daroux M L, Faguy P W and Yeager E 1987 Identification of surface-films formed on lithium in propylene carbonate solutions *J. Electrochem. Soc.* **134** 1611–20

[206] Aurbach D, Zinigrad E, Cohen Y and Teller H 2002 A short review of failure mechanisms of lithium metal and lithiated graphite anodes in liquid electrolyte solutions *Solid State Ion.* **148** 405–16

[207] Shi Z, Liu M, Naik D and Gole J L 2001 Electrochemical properties of Li–Mg alloy electrodes for lithium batteries *J. Power Sources* **92** 70–80

[208] Suresh P, Shukla A K, Shivashankar S A and Munichandraiah N 2004 Rechargeable lithium cells with dendrite-free electrodeposited lithium on aluminium as negative electrode *J. Power Sources* **132** 166–71

[209] Stark J K, Ding Y and Kohl P A 2011 Dendrite-free electrodeposition and reoxidation of lithium–sodium alloy for metal-anode battery *J. Electrochem. Soc.* **158** A1100–5

[210] Schweikert N *et al* 2013 Suppressed lithium dendrite growth in lithium batteries using ionic liquid electrolytes: investigation by electrochemical impedance spectroscopy, scanning electron microscopy, and *in situ* ^{7}Li nuclear magnetic resonance spectroscopy *J. Power Sources* **228** 237–43

[211] Suo L, Hu Y-S, Li H, Armand M and Chen L 2013 A new class of Solvent-in-Salt electrolyte for high-energy rechargeable metallic lithium batteries *Nat. Commun.* **4** 1481

[212] Ding F *et al* 2013 Dendrite-free lithium deposition via self-healing electrostatic shield mechanism *J. Am. Chem. Soc.* **135** 4450–6

[213] Zhang Y *et al* 2014 Dendrite-free lithium deposition with self-aligned nanorod structure *Nano Lett.* **14** 6889–96

[214] Xu W *et al* 2014 Lithium metal anodes for rechargeable batteries *Energy Environ. Sci.* **7** 513–37

[215] Aurbach D, Weissman I, Zaban A and Chusid O 1994 Correlation between surface chemistry, morphology, cycling efficiency and interfacial properties of Li electrodes in solutions containing different Li salts *Electrochim. Acta* **39** 51–71

[216] Wan C *et al* 2017 Multinuclear NMR study of the solid electrolyte interface formed in lithium metal batteries *ACS Appl. Mater. Interfaces* **9** 14741–8

[217] Vijayakumar M *et al* 2009 Combined ^{6,7}Li NMR and molecular dynamics study of Li diffusion in Li_2TiO_3 *J. Phys. Chem.* C **113** 20108–16

[218] Deng X C *et al* 2016 Nuclear magnetic resonance studies of the solvation structures of a high-performance nonaqueous redox flow electrolyte *J. Power Sources* **308** 172–9

[219] Wan C *et al* 2016 Natural abundance ^{17}O, ^{6}Li NMR and molecular modeling studies of the solvation structures of lithium bis(fluorosulfonyl)imide/1,2-dimethoxyethane liquid electrolytes *J. Power Sources* **307** 231–43

[220] Hu M Y *et al* 2016 *In situ* natural abundance ^{17}O and ^{25}Mg NMR investigation of aqueous $Mg(OH)_2$ dissolution in the presence of supercritical CO_2 *Environ. Sci. Technol.* **50** 12373–84

[221] Pour N, Gofer Y, Major D T and Aurbach D 2011 Structural analysis of electrolyte solutions for rechargeable Mg batteries by stereoscopic means and DFT calculations *J. Am. Chem. Soc.* **133** 6270–8

[222] Muldoon J, Bucur C B, Oliver A G, Zajicek J, Allred G D and Boggess W C 2013 Corrosion of magnesium electrolytes: chlorides—the culprit *Energy Environ. Sci.* **6** 482–7

[223] Saha P, Datta M K, Velikokhatnyi O I, Manivannan A, Alman D and Kumta P N 2014 Rechargeable magnesium battery: current status and key challenges for the future *Prog. Mater. Sci.* **66** 1–86

[224] Aurbach D, Weissman I, Gofer Y and Levi E 2003 Nonaqueous magnesium electrochemistry and its application in secondary batteries *Chem. Rec.* **3** 61–73

[225] Aurbach D *et al* 2001 A comparison between the electrochemical behavior of reversible magnesium and lithium electrodes *J. Power Sources* **97–8** 269–73

[226] Muldoon J, Bucur Claudiu B and Gregory T 2017 Fervent hype behind magnesium batteries: an open call to synthetic chemists—electrolytes and cathodes needed *Angew. Chem., Int. Ed.* **56** 12064–84

[227] Wei X *et al* 2015 Towards high-performance nonaqueous redox flow electrolyte via ionic modification of active species *Adv. Energy Mater.* **5** 1400678
[228] Kalita M *et al* 2005 Effect of calixpyrrole in PEO–$LiBF_4$ polymer electrolytes *Electrochim. Acta* **50** 3942–8
[229] Wieczorek W, Zukowska G, Borkowska R, Chung S H and Greenbaum S 2001 A basic investigation of anhydrous proton conducting gel electrolytes *Electrochim. Acta* **46** 10–11 1427–38
[230] Chung S H *et al* 2001 Enhancement of ion transport in polymer electrolytes by addition of nanoscale inorganic oxides *J. Power Sources* **97–8** 644–8
[231] Wang Y Y *et al* 2013 Examination of methods to determine free-ion diffusivity and number density from analysis of electrode polarization *Phys. Rev.* E **87** 042308
[232] Vijayakumar M, Han K S, Hu J and Mueller K T 2017 Molecular level structure and dynamics of electrolytes using ^{17}O nuclear magnetic resonance spectroscopy *eMagRes* **6** 71–82
[233] Ilott A J, Mohammadi M, Chang H J, Grey C P and Jerschow A 2016 Real-time 3D imaging of microstructure growth in battery cells using indirect MRI *Proc. Natl Acad. Sci.* **113** 10779
[234] Chandrashekar S, Trease N M, Chang H J, Du L S, Grey C P and Jerschow A 2012 Li-7 MRI of Li batteries reveals location of microstructural lithium *Nat. Mater.* **11** 311–5
[235] Li Z, Huang J, Yann Liaw B, Metzler V and Zhang J 2014 A review of lithium deposition in lithium-ion and lithium metal secondary batteries *J. Power Sources* **254** 168–82
[236] Ilott A J, Mohammadi M, Schauerman C M, Ganter M J and Jerschow A 2018 Rechargeable lithium-ion cell state of charge and defect detection by *in situ* inside-out magnetic resonance imaging *Nat. Commun.* **9** 1776
[237] Krachkoyskiy S A, Pauric A D, Halalay I C and Goward G R 2013 Slice-selective NMR diffusion measurements: a robust and reliable tool for *in situ* characterization of ion-transport properties in lithium-ion battery electrolytes *J. Phys. Chem. Lett.* **4** 3940–4
[238] Gunther W R, Michaelis V K, Caporini M A, Griffin R G and Román-Leshkov Y 2014 Dynamic nuclear polarization NMR enables the analysis of sn-beta zeolite prepared with natural abundance ^{119}Sn precursors *J. Am. Chem. Soc.* **136** 6219–22
[239] Blanc F, Sperrin L, Jefferson D A, Pawsey S, Rosay M and Grey C P 2013 Dynamic nuclear polarization enhanced natural abundance ^{17}O spectroscopy *J. Am. Chem. Soc.* **135** 2975–8
[240] Prandolini M J, Denysenkov V P, Gafurov M, Endeward B and Prisner T F 2009 High-field dynamic nuclear polarization in aqueous solutions *J. Am. Chem. Soc.* **131** 6090–2